ARMY RESEARCH LABORATORY

Through the Wall Radar Simulations Using Polarimetric Antenna Patterns

by Traian Dogaru and Calvin Le

ARL-TR-5951 **March 2012**

NOTICES

Disclaimers

The findings in this report are not to be construed as an official Department of the Army position unless so designated by other authorized documents.

Citation of manufacturer's or trade names does not constitute an official endorsement or approval of the use thereof.

Destroy this report when it is no longer needed. Do not return it to the originator.

Army Research Laboratory
Adelphi, MD 20783-1197

ARL-TR-5951 **March 2012**

Through the Wall Radar Simulations Using Polarimetric Antenna Patterns

Traian Dogaru and Calvin Le
Sensors and Electron Devices Directorate, ARL

REPORT DOCUMENTATION PAGE	Form Approved OMB No. 0704-0188

PLEASE DO NOT RETURN YOUR FORM TO THE ABOVE ADDRESS.

1. REPORT DATE *(DD-MM-YYYY)*	2. REPORT TYPE	3. DATES COVERED (From - To)
March 2012	Final	2011

4. TITLE AND SUBTITLE

Through the Wall Radar Simulations Using Polarimetric Antenna Patterns

5a. CONTRACT NUMBER

5b. GRANT NUMBER

5c. PROGRAM ELEMENT NUMBER

6. AUTHOR(S)

Traian Dogaru and Calvin Le

5d. PROJECT NUMBER

5e. TASK NUMBER

5f. WORK UNIT NUMBER

7. PERFORMING ORGANIZATION NAME(S) AND ADDRESS(ES)

U.S. Army Research Laboratory
ATTN: RDRL-SER-U
2800 Powder Mill Road
Adelphi, MD 20783-1197

8. PERFORMING ORGANIZATION REPORT NUMBER

ARL-TR-5951

9. SPONSORING/MONITORING AGENCY NAME(S) AND ADDRESS(ES)

10. SPONSOR/MONITOR'S ACRONYM(S)

11. SPONSOR/MONITOR'S REPORT NUMBER(S)

12. DISTRIBUTION/AVAILABILITY STATEMENT

Approved for public release; distribution unlimited.

13. SUPPLEMENTARY NOTES

14. ABSTRACT

In this report, we analyze the impact of coupling the polarimetric characteristics of antennas and targets on a radar system response and performance. We start by formulating the basic equations that govern this interaction and extend them to images created by an ultra-wideband (UWB), broad-beam-antenna, strip-map synthetic aperture radar (SAR) system. In the numerical example section, we apply this method to the problem of through-the-wall detection of a small weapon based on polarimetric differences between SAR images. The scenarios considered involve buildings of various complexities, as well as two families of antenna patterns. The results demonstrate a reduction in the weapon detection scheme performance when the radar antenna cross-polarization suppression drops under a certain limit. The numerical examples are based on simulated data obtained by the AFDTD software (for the radar target signature) and the FEKO software (for the antenna patterns).

15. SUBJECT TERMS

Sensing through the wall, polarimetric radar, computational electromagnetics

16. SECURITY CLASSIFICATION OF:			17. LIMITATION OF ABSTRACT	18. NUMBER OF PAGES	19a. NAME OF RESPONSIBLE PERSON
a. REPORT	b. ABSTRACT	c. THIS PAGE			Traian Dogaru
UNCLASSIFIED	UNCLASSIFIED	UNCLASSIFIED	UU	56	19b. TELEPHONE NUMBER (*Include area code*) (301) 394-1482

Standard Form 298 (Rev. 8/98)
Prescribed by ANSI Std. Z39.18

Contents

List of Figures

List of Tables

INTENTIONALLY LEFT BLANK.

Acknowledgments

The authors would like to acknowledge the contributions of Dr. Christopher Kenyon and Dr. DaHan Liao, both from the U.S. Army Research Laboratory (ARL). Dr. Kenyon provided the FEKO-simulated data for the Synchronous Impulse Reconstruction (SIRE) radar transmitting antenna patterns, while Dr. Liao provided the FEKO-simulated data for the SIRE radar receiving antenna patterns.

INTENTIONALLY LEFT BLANK.

1. Introduction

The Radio Frequency (RF) Signal Processing and Modeling Branch at the U.S. Army Research Laboratory (ARL) has been involved in the Army's development efforts in Sensing through the Wall (STTW) radar technology for several years. A significant part of our work consisted of modeling radar systems for complex building imaging, with the purpose of understanding the radar scattering phenomenology, developing image formation algorithms, and studying design parameter trade-offs. A previous technical report (*1*) suggested a method for detecting behind-the-wall humans carrying small weapons based on polarimetric radar signature. The proposed technique was supported by computer models of the radar scattering scenario. However, as pointed out in (*1*), that study contained a number of simplifying assumptions that could have had a large impact on the expected performance of such detection method. The current report attempts to remedy these shortcomings by bringing more realistic features into the modeling scenario.

One of the major assumptions in most of our electromagnetic (EM) scattering models is that the radar targets are placed in the far-field region (*2*) relative to the transmitter and receiver. As a consequence, both the fields incident on the target and the scattered fields observed at the receiver are considered plane waves. Additionally, the excitation plane waves have equal amplitudes, regardless of the incidence angle. While this model is a very good approximation of many radar sensing scenarios, there are situations where the transmitter and receiver antenna patterns play an important role. Moreover, the targets may be placed in the transmitter's or receiver's near-field region, invalidating the far-field assumption. An example of such geometry is provided by a ground vehicle-based radar system for building imaging that operates in a side-looking, strip-map synthetic aperture radar (SAR) mode (*3*), which is relevant to the STTW radar technology currently developed by the Army. This study demonstrates how the far-field, plane-wave EM computer models can be adapted to closely simulate a strip-map SAR scenario using wide-beam antenna patterns.

An additional complication is introduced by coupling between the polarimetric characteristics of the antenna radiation and target scattering. While this issue generally applies to single polarization radar, it becomes critical to a fully polarimetric radar system, such as the one considered in (*1*). A similar problem was first investigated in (*4*) and has subsequently received significant attention in the remote sensing community (*5*–*10*). Most of these papers deal with the issue of polarimetric radar calibration, in which measured radar data are processed to remove the antenna cross-polarization contamination, thereby providing a more accurate polarimetric characterization of the target. This can be regarded as an inverse problem, in which information about the target is extracted from the observed data. Our approach in this report consists of solving the forward problem, where we assume we have complete knowledge of the system

parameters, the targets, and the environment around them, and attempt to predict the performance of the uncompensated radar system and signal processing algorithms.

Although the theoretical formulation of the polarimetric coupling between antennas and target can be found in many of the references already mentioned, we present a complete derivation of the equations that govern this coupling and quantify its importance on the polarimetric performance of a radar imaging system. Finally, we apply this formulation to the problem of through-the-wall small weapon detection via polarimetric radar and show how the detection performance is affected by introducing more realistic assumptions about the radar system and geometry.

The report is organized as follows: in section 2, we develop the theoretical formulation of the modeling method for polarimetric radar imaging; in section 3, we present numerical results for scenarios with increasing degrees of complexity; in section 4, we draw conclusions and indicate possible improvements of the method.

2. Theoretical Formulation

2.1 Modeling a SAR Imaging System

In previous work (*11, 12*) we discussed the tools and methods used at ARL to model SAR systems for STTW building imaging. The computational electromagnetic (CEM) code we rely on for most of our EM simulations is AFDTD (*13*), which was entirely developed at ARL and implements the finite-difference time-domain technique. A comprehensive description of the underlying computational method for this code can be found in (*14*). In (*11*), we also described the basic SAR system geometries, namely spotlight and strip-map, and their relationship to the numerical scattering models provided by the CEM codes. Thus, we established the fact that the far-field geometry assumption of the AFDTD models is generally consistent with most spotlight SAR systems and discussed the transformations on these models that are needed in order to emulate a strip-map SAR system. In this section, we elaborate further on this topic.

Let us consider the most basic geometries of spotlight (figure 1a) and strip-map (figure 1b) SAR systems. We make a number of simplifying assumptions to our scenarios: the radar and its trajectory, the target, and the image are all placed in the horizontal (x-y) plane; the target is in the radar's far-field region; the transmitter and receiver are collocated (monostatic configuration); there is no variation of the radar antenna patterns with the elevation angle θ measured from the horizontal plane; the entire configuration is placed in free-space (no physical ground plane); and we consider only one polarization. Characteristic to the spotlight configuration is that the antenna beam always points toward one point in the image (called focus) as the radar moves along the synthetic aperture. At the same time, in a strip-map configuration, the antenna beam always

points in the same direction. Ideally, the spotlight radar illuminates the area of interest with plane waves (narrow beams), whereas the strip-map radar operates with broad antenna beams.

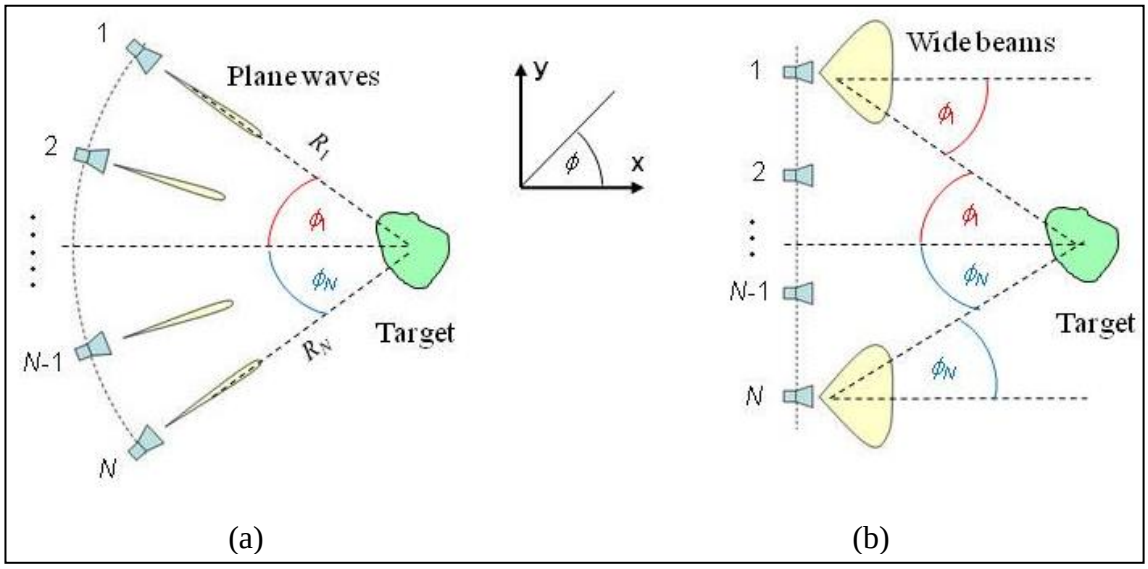

Figure 1. Schematic representation of a SAR imaging system geometry in two different configuration: (a) spotlight; (b) strip-map.

In the following, we assume that the SAR image is created by the back-projection algorithm (BPA) (*15*). We also assume that the imaging algorithm does not compensate for the path loss (the variation of the radar return magnitude with range); therefore, the particular shape of the radar trajectory along the synthetic aperture is irrelevant. Under these assumptions, for the spotlight configuration, the image pixel intensity in the target neighborhood can be written as:

$$I(x,y)=\sum_{n=1}^{N} w(\phi_n)s_n(\tau_n(x,y)), \tag{1}$$

where $w(\phi)$ is a post-processing angular window, $s_n(t)$ is the time-domain scattered signal received at position *n*, and $\tau_n(x,y)$ is the propagation delay from the radar position *n* to the image point of coordinates (x,y):

$$\tau_n(x,y)=\frac{2[R_n-(x\cos\phi_n+y\sin\phi_n)]}{c}, \tag{2}$$

where R_n and ϕ_n are the range and angle of the radar position *n* with respect to the coordinate origin of the image. Notice that, consistent with the far-field assumption, all the pixels in the image "see" the radar in position *n* at the same azimuth angle ϕ_n. For the strip-map configuration, the image pixel intensity is given by:

$$I(x,y)=\sum_{n=1}^{N} p(\phi_n)s_n(\tau_n(x,y)) \tag{3}$$

where the function $p(\phi)$ describes the antenna pattern (or, more rigorously, the combined transmit and receive antenna patterns). It is easy to see that the two formulations (described by equations 1 and 3) can be made equivalent if we replace $w(\phi)$ by $p(\phi)$.

The AFDTD code provides the radar returns $s_n(t)$ for various incidence and observation angles ϕ. In previous work (*11–12*), we considered the spotlight imaging geometry and applied a generic angular window (such as Hanning [*16*]), primarily with the purpose of reducing the image sidelobes. However, the imaging algorithm based on AFDTD scattering data can be adapted to closely emulate the strip-map geometry if we simply consider the antenna pattern $p(\phi)$ instead of the window function $w(\phi)$, according to equation 3.

The simplifying assumptions introduced earlier in this section can be eliminated at the expense of a more cumbersome formulation. Thus, if one considers a bistatic radar configuration, the summation in equations 1 and 3 must be performed over all pairs of transmitter-receiver locations. Using index *n* for such a pair location, and (R_{Tn}, ϕ_{Tn}) and (R_{Rn}, ϕ_{Rn}) for the range and angle of the transmitter and receiver, respectively, the propagation delay becomes:

$$\tau_n(x,y) = \frac{\left[R_{Tn} - \left(x\cos\phi_{Tn} + y\sin\phi_{Tn}\right)\right] + \left[R_{Rn} - \left(x\cos\phi_{Rn} + y\sin\phi_{Rn}\right)\right]}{c} \tag{4}$$

The restrictions regarding the radar aperture, target, and image in the horizontal plane, as well as the free-space assumption, can be easily overcome by considering imaging in a slant plane over an infinite ground plane (the AFDTD code can readily provide scattering data for such a configuration). Additionally, the antenna pattern elevation variation can also be accounted for, according to the following equations (valid for monostatic configuration):

$$I(x,y,z) = \sum_{n=1}^{N} p(\theta_n, \phi_n) s_n(\tau_n(x,y,z)) \tag{5}$$

$$\tau_n(x,y,z) = \frac{2\left[R_n - \left(x\cos\phi_n\cos\theta_n + y\sin\phi_n\cos\theta_n + z\sin\theta_n\right)\right]}{c} \tag{6}$$

The issue of wave polarization will be considered in the next two sections. However, the distinction between near-field vs. far-field geometry cannot be resolved within the framework developed in this section. In order to model the near-field scenario rigorously, a near-field EM scattering code is required, while the SAR image formation algorithm must be reformulated to include the exact Euclidian distance between the image pixel and the radar position coordinates.

We also need to mention that throughout this report, the SAR images are created with the polar format algorithm (PFA) (*17*) instead of the BPA. However, it can be shown (*18*) that for a spotlight SAR system operating in the far-field, the two formulations are equivalent since they both amount to a two-dimensional (2-D) inverse Fourier transform from the frequency-angle space to the image space. In light of the previous considerations, we can then model a strip-map

geometry using BPA by applying the antenna patterns to the PFA based on spotlight (or AFDTD-modeled) data.

2.2 Accounting for the Polarization Coupling between Radar Antennas and Target

Consider the radar scattering scenario illustrated in figure 2, where, for maximum generality, we describe a bistatic configuration. The relative range and angles from the transmitter to the target are R_T, θ_T, and ϕ_T, respectively, whereas the relative range and angles from the target to the receiver are R_R, θ_R, and ϕ_R (throughout this report we use the *T* subscript for transmitter and the *R* subscript for receiver).

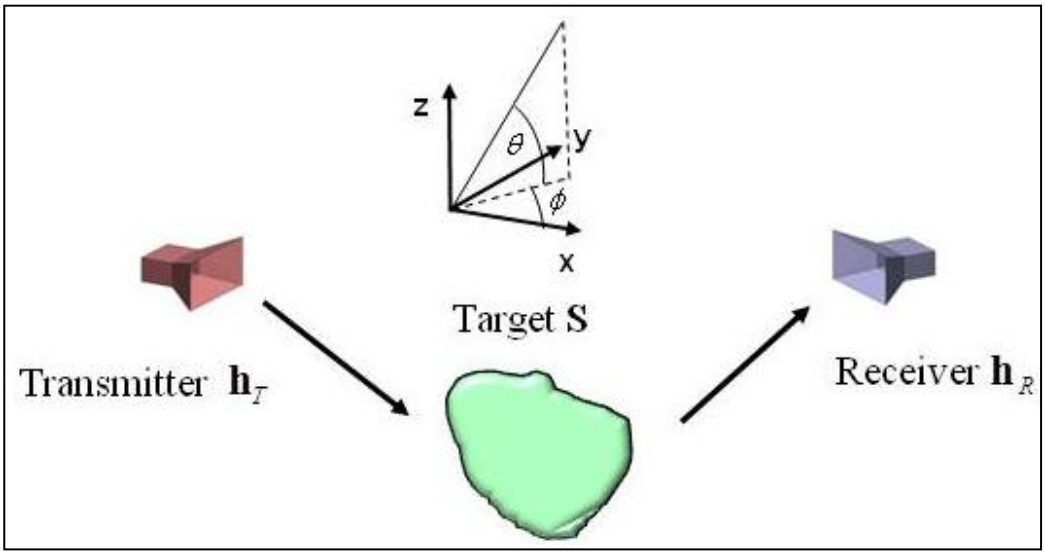

Figure 2. Schematic representation of a bistatic radar scattering scenario, showing generic transmitting and receiving radar antennas.

In the previous section, we assumed that the radar antennas transmit and receive only one polarization. While most radar antennas are designed to work in one principal polarization (also called co-polarization), cross-polarization fields (orthogonal to co-polarization) are also generally present in the radiation pattern. Therefore, the far-zone electric field of a radiating antenna can be represented as a 2-D vector [(*9]*)

$$\mathbf{E}_T\left(R_T,\theta_T,\phi_T\right)=\begin{bmatrix}E_{TV}\\E_{TH}\end{bmatrix}=\frac{jZ_0I}{2\lambda R_T}e^{-jkR_T}\begin{bmatrix}h_{TV}\\h_{TH}\end{bmatrix}=\frac{jZ_0I}{2\lambda R_T}e^{-jkR_T}\mathbf{h}_T\left(\theta_T,\phi_T\right), \tag{7}$$

where Z_0 is the free-space impedance, I is the current at the antenna terminals, λ is the wavelength, and k is the wavenumber. The vector **h**, called effective length of the antenna (*19, 20*), can be decomposed along any two orthogonal directions perpendicular to the $\mathbf{u}_R$ unit vector. Typically, the two components are written as h_θ and h_ϕ, which are the projections along the unit vectors $\mathbf{u}_\theta$ and $\mathbf{u}_\phi$. Throughout this report, we will use the notations h_V and h_H, whereas by the

subscript *V* (vertical) we understand the component along $\mathbf{u}_\theta$ and by the subscript *H* (horizontal) we understand the component along $\mathbf{u}_\phi$. Notice that in equation 7, the elements of the vector **h** capture entirely the angular dependence of the radiated electric field vector $\mathbf{E}_T$.

The polarimetric far-zone electric field scattered by the target that reaches the receiving antenna is characterized by the following equation (*21*):

$$\mathbf{E}_R(R_R,\theta_R,\phi_R)=\frac{e^{-jkR_R}}{R_R}\mathbf{S}(\theta_T,\phi_T,\theta_R,\phi_R)\mathbf{E}_T(R_T,\theta_T,\phi_T), \tag{8}$$

or, in matrix form:

$$\begin{bmatrix} E_{RV} \\ E_{RH} \end{bmatrix}=\frac{e^{-jkR_R}}{R_R}\begin{bmatrix} S_{VV} & S_{VH} \\ S_{HV} & S_{HH} \end{bmatrix}\begin{bmatrix} E_{TV} \\ E_{TH} \end{bmatrix}. \tag{9}$$

In equation (8), **S** is called the scattering matrix of the target. Finally, the open-circuit voltage at the receiver antenna is given by (*19, 20*):

$$V=\mathbf{h}_R^{\mathrm{T}}(\theta_R,\phi_R)\mathbf{E}_R(R_R,\theta_R,\phi_R)=\begin{bmatrix} h_{RV} & h_{RH} \end{bmatrix}\begin{bmatrix} E_{RV} \\ E_{RH} \end{bmatrix} \tag{10}$$

where the superscript T stands for the transposed matrix. By combining equations 7, 8 and 10 we obtain:

$$V=\frac{jZ_0I}{2\lambda R_T R_R}e^{-jk(R_T+R_R)}\mathbf{h}_R^{\mathrm{T}}(\theta_R,\phi_R)\mathbf{S}(\theta_T,\phi_T,\theta_R,\phi_R)\mathbf{h}_T(\theta_T,\phi_T) \tag{11}$$

or, in a more explicit form:

$$V=\frac{jZ_0I}{2\lambda R_T R_R}e^{-jk(R_T+R_R)}\begin{bmatrix} h_{RV} & h_{RH} \end{bmatrix}\begin{bmatrix} S_{VV} & S_{VH} \\ S_{HV} & S_{HH} \end{bmatrix}\begin{bmatrix} h_{TV} \\ h_{TH} \end{bmatrix} \tag{12}$$

At this point, we need to examine the factors that appear in the right side of equation (11), their dependence on various parameters, and their importance in creating ultra-wideband (UWB) broad-beam-antenna SAR images of the target. The relevant parameters for calculating the received open-circuit voltage are the ranges (R_T and R_R), the angles (θ_T, ϕ_T, θ_R, and ϕ_R), and the frequency (expressed in equation 11 by λ, but also implicitly by $\mathbf{h}_R$, **S** and $\mathbf{h}_T$). The formation of far-field SAR images as outlined in section 2.1 involves neglecting the factors containing the ranges (including the phase factor $e^{-jk(R_T+R_R)}$), and keeping only the factors that express the dependence on angles and frequency (namely, $\mathbf{h}_R$, **S** and $\mathbf{h}_T$ and λ).

Now let us define the normalized effective length of the antenna as:

$$\boldsymbol{\eta}=\begin{bmatrix} \eta_V \\ \eta_H \end{bmatrix}=\frac{1}{\lambda}\begin{bmatrix} h_V \\ h_H \end{bmatrix}=\frac{1}{\lambda}\mathbf{h}. \tag{13}$$

Equation 11 becomes:

$$V = \frac{jZ_0 I}{2}\frac{\lambda}{R_T R_R} e^{-jk(R_T+R_R)} \boldsymbol{\eta}_R^{\mathrm{T}}(\theta_R,\phi_R)\mathbf{S}(\theta_T,\phi_T,\theta_R,\phi_R)\boldsymbol{\eta}_T(\theta_T,\phi_T). \tag{14}$$

Since the received power is proportional to $|V|^2$, while the transmitted power is proportional to $|I|^2$ (with the proportionality factors independent of ranges, angles and frequency), we can write the relationship between transmitted and received power as:

$$P_R = P_T C_1 \left(\frac{\lambda}{R_T R_R}\right)^2 \left|\boldsymbol{\eta}_R^{\mathrm{T}}(\theta_R,\phi_R)\mathbf{S}(\theta_T,\phi_T,\theta_R,\phi_R)\boldsymbol{\eta}_T(\theta_T,\phi_T)\right|^2, \tag{15}$$

where the constant C_1 does not depend on ranges, angles, or frequency. The classic radar equation as formulated in (*20*) can be written as:

$$P_R = P_T C_2 \left(\frac{\lambda}{R_T R_R}\right)^2 G_R(\theta_R,\phi_R)\sigma(\theta_T,\phi_T,\theta_R,\phi_R)G_T(\theta_T,\phi_T)\left|\hat{\boldsymbol{\rho}}_W \cdot \hat{\boldsymbol{\rho}}_R\right|^2, \tag{16}$$

where G_T and G_R are the transmitting and receiving antenna gains, respectively, σ is the radar cross section (RCS), $\hat{\boldsymbol{\rho}}_W$ is the polarization unit vector of the scattered waves, and $\hat{\boldsymbol{\rho}}_R$ is the polarization unit vector of the receiving antenna. Notice the close resemblance between equations 15 and 16, with the factor $\left|\boldsymbol{\eta}_R^{\mathrm{T}}(\theta_R,\phi_R)\mathbf{S}(\theta_T,\phi_T,\theta_R,\phi_R)\boldsymbol{\eta}_T(\theta_T,\phi_T)\right|^2$ accounting for antenna gain and polarization and target RCS. In the remainder of this study, the SAR image formation algorithms will use the quantity defined by $\boldsymbol{\eta}_R^{\mathrm{T}}(\theta_R,\phi_R)\mathbf{S}(\theta_T,\phi_T,\theta_R,\phi_R)\boldsymbol{\eta}_T(\theta_T,\phi_T)$, which captures the entire dependence on the angles θ_T, ϕ_T, θ_R, and ϕ_R, together with a frequency dependence consistent with the radar equation.

2.3 Formulation for a Fully Polarimetric Radar System

A fully polarimetric radar system (*19*) includes pairs of antennas that can transmit and receive both orthogonal polarizations, as shown schematically in figure 3. We use the superscript *V* to indicate a vertically polarized transmitting or receiving antenna and the superscript *H* for a horizontally polarized antenna (here, the terms "vertical" or "horizontal" describe the antenna's principal polarization). In most of our previous modeling work (*11*, *12*) based on AFDTD computer simulations, we characterized the radar signature of targets by the matrix **S**, which assumes purely *V* or *H*-polarized plane waves both at transmission and reception. However, since the antennas generally transmit and receive both co- and cross-polarized fields, the characterization of the polarimetric radar system described in figure 3 extends beyond the target scattering matrix and must include the antenna polarization properties.

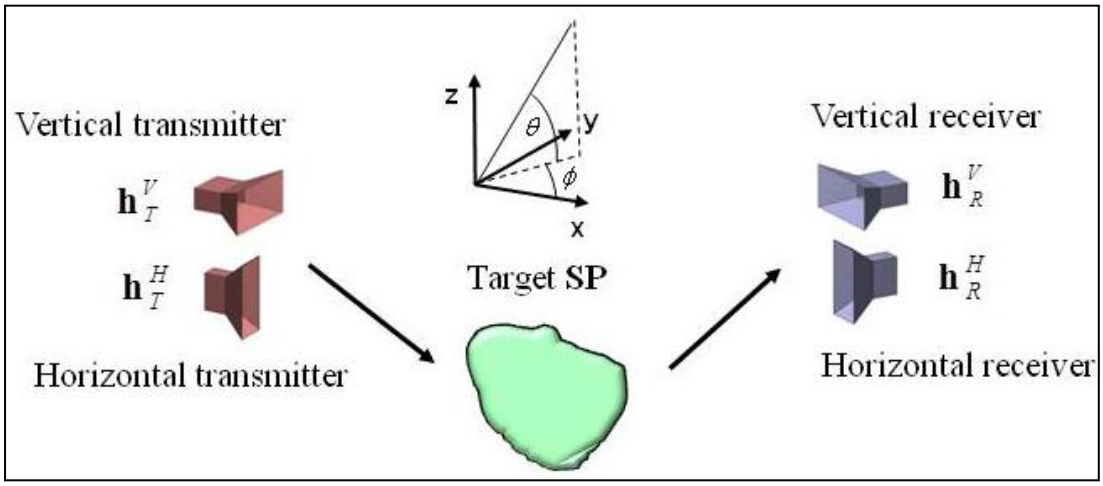

Figure 3. Schematic representation of a fully polarimetric radar scattering scenario, showing the vertically and horizontally polarized, transmitting and receiving radar antennas.

For the polarimetric radar system that includes the antennas, we introduce the scattering matrix **SA** defined as:

$$\mathbf{SA} = \begin{bmatrix} SA_{VV} & SA_{VH} \\ SA_{HV} & SA_{HH} \end{bmatrix}, \tag{17}$$

where, for instance, SA_{VV} stands for the element characterizing vertical antenna polarization at both transmission and reception. We also replace the notation for the previously described scattering matrix **S** (that considers plane waves only) with **SP**. Then, based on the formulation developed in section 2.2, we can write:

$$\begin{bmatrix} SA_{VV} & SA_{VH} \\ SA_{HV} & SA_{HH} \end{bmatrix} = \begin{bmatrix} \eta_{RV}^V & \eta_{RH}^V \\ \eta_{RV}^H & \eta_{RH}^H \end{bmatrix} \begin{bmatrix} SP_{VV} & SP_{VH} \\ SP_{HV} & SP_{HH} \end{bmatrix} \begin{bmatrix} \eta_{TV}^V & \eta_{TV}^H \\ \eta_{TH}^V & \eta_{TH}^H \end{bmatrix} \tag{18}$$

or, in a more compact form:

$$\mathbf{SA} = \mathbf{P}_R^{\mathrm{T}} (\mathbf{SP}) \mathbf{P}_T , \tag{19}$$

where the matrices $\mathbf{P}_T$ and $\mathbf{P}_R$ characterize the pairs of antennas at the transmitter and receiver, respectively (these are called "distortion matrices" in [*5–7*]). The voltages received by the four possible polarimetric antenna combinations would then be proportional to the elements of **SA**. Notice that all the quantities involved in equation 18 depend only on angles θ_T, ϕ_T, θ_R, and ϕ_R, and frequency, but not on ranges.

The **SA** scattering matrix introduced by equation 19 effectively replaces the original **SP** scattering matrix (obtained under the plane-wave assumption) by accounting for the variation of the radar return with the relative pairs of angles (θ_T, ϕ_T, θ_R, and ϕ_R) between antennas and target.

Importantly, since the η elements are non-dimensional, the **SA** and **SP** elements have the same dimensionality (namely, meters).

Antenna-normalized effective lengths of form η_V^V and η_H^H characterize the co-polarization fields of the antennas, whereas the normalized effective lengths of form η_V^H and η_H^V characterize the cross-polarization fields of the antennas. In general, we call the ratio between the magnitudes of the co- and cross-polarization elements of the vector $\boldsymbol{\eta}$ of an antenna the polarization ratio *PR* of that antenna. Thus, for the vertically polarized antennas (transmitting or receiving), we have:

$$PR = \frac{\left|\eta_V^V\right|}{\left|\eta_H^V\right|}, \tag{20}$$

whereas, for the horizontally polarized antennas, we have:

$$PR = \frac{\left|\eta_H^H\right|}{\left|\eta_V^H\right|} \tag{21}$$

Let us rewrite two elements of the matrix described in equation 18 separately:

$$SA_{VV} = \eta_{RV}^V SP_{VV} \eta_{TV}^V + \eta_{RV}^V SP_{VH} \eta_{TH}^V + \eta_{RH}^V SP_{HV} \eta_{TV}^V + \eta_{RH}^V SP_{HH} \eta_{TH}^V \tag{22}$$

$$SA_{VH} = \eta_{RV}^V SP_{VV} \eta_{TV}^H + \eta_{RV}^V SP_{VH} \eta_{TH}^H + \eta_{RH}^V SP_{HV} \eta_{TV}^H + \eta_{RH}^V SP_{HH} \eta_{TH}^H . \tag{23}$$

By examining equations 22 and 23, we notice that, in each element of **SA**, all elements of **SP** appear coupled by the antenna-normalized effective length vectors $\boldsymbol{\eta}$. When the polarization ratios of the antennas are large, the elements of the matrix **SA** are closer to the elements of the matrix **SP** (which assumes purely polarized plane waves). In the opposite case, when the polarization ratios of the antennas are relatively small (meaning strong cross-polarization components in the antenna patterns are present), there is generally a reduction in the polarimetric differences between the elements of **SA** as compared to those of **SP**. Therefore, a radar system that relies on certain particular properties of the target scattering matrix **SP** may see a reduction in performance when it operates with antennas that exhibit low polarization ratios.

Since the elements of the normalized effective length vector $\boldsymbol{\eta}$ depend on the angles θ and ϕ, it follows that the polarization ratio of an antenna also depends on these angles. In low-frequency (1–4 GHz), UWB strip-map SAR imaging systems used in STTW applications, broad beam antennas are typically employed in order to achieve large integration angles and satisfactory cross-range resolution (*11*). Therefore, when we characterize the polarization performance of an antenna for these applications, we need to take into account the variation of *PR* over the angles of interest, both in elevation and azimuth. One possible metric for polarization performance is the root mean square (RMS) of the polarization ratio:

$$PR_{RMS} = \frac{\sqrt{\int_{\phi_1}^{\phi_2}\int_{\theta_1}^{\theta_2} \left|\eta_{co-pol}(\theta,\phi)\right|^2 d\theta d\phi}}{\sqrt{\int_{\phi_1}^{\phi_2}\int_{\theta_1}^{\theta_2} \left|\eta_{cross-pol}(\theta,\phi)\right|^2 d\theta d\phi}}, \quad (24)$$

where the integration is performed over the ranges of θ and ϕ that are considered in the image formation algorithm.

Additionally, the polarization ratio of an antenna may depend on frequency. In typical antenna configurations, PR_{RMS} is large at low frequencies and becomes smaller as the frequency increases (*20*). Since our STTW SAR application involves wide frequency ranges, we will use the PR_{RMS} in the center of the bandwidth as the final antenna polarization performance metric.

2.4 Typical Radar Antenna Patterns

It is useful to illustrate the discussion on polarimetric antenna patterns with a representative example. In this section, we plot the 2-D and three-dimensional (3-D) patterns of a hypothetical antenna that approximate the free-space, far-field radiation of an open rectangular waveguide operating in the TE_{10} (fundamental) mode, backed by an infinite metallic ground plane (*20*). The equations describing these patterns are given in section 3.2, together with details on the antenna geometry. We also assume that the aperture is oriented such that the principal polarization is vertical. It should be mentioned that, although this type of antenna is not frequently used in practice, the general shape of its patterns is fairly representative for a large number of linearly polarized radar antennas, such as the horn or Vivaldi antennas (*20, 22*).

The 3-D antenna patterns at 4.5 GHz are shown in figure 4, for the co-polarization or vertical (figure 4a) and the cross-polarization or horizontal (figure 4b) electric field components, which are proportional to the vertical and horizontal components of the $\boldsymbol{\eta}$ vector, respectively. The pseudo-color maps represent dB values of the electric field magnitude. The absolute electric field intensity values, as well as the conversion factor from electric field to normalized effective length $\boldsymbol{\eta}$, is irrelevant for our discussion. In all cases, only the forward-directed ($x > 0$) patterns are plotted.

Typical for the co-polarization antenna pattern displayed in figure 4a is the main lobe present around the boresight direction ($\theta = 0^o$ and $\phi = 0^o$), while multiple sidelobes of reduced intensity extend in both vertical and horizontal directions. The width of the main lobe generally varies inverse proportionally with the operating frequency. For the cross-polarization pattern (figure 4b), we also notice the presence of multiple lobes in both vertical and horizontal directions; however, characteristically, there are nulls in this pattern along both the $\theta = 0^o$ and the $\phi = 0^o$ planes. Following the usual antenna terminology, the $\phi = 0^o$ (vertical) plane is called the "E-plane," whereas the $\theta = 0^o$ (horizontal) plane is called the "H-plane" (*20*). The fact that the cross-

polarization fields radiated in the E- and H-planes are null follows from the symmetry properties of the antenna geometry and is typical for many idealized radar antenna designs.

To illustrate the behavior of the antenna radiation in the vicinity of the E- and H-planes we plotted the 2-D patterns in polar coordinates in figure 5. Thus, figure 5a shows the co- and cross-polarization patterns in the $\phi = 5^{o}$ plane (close to the E-plane), whereas figure 5b shows the patterns in the $\theta = 5^{o}$ plane (close to the H-plane). Notice that we avoided showing the patterns that characterize the exact E- and H-planes, because, in those planes, the cross-polarization fields would be null (consequently, the polarization ratio *PR* would be infinity). The plots in figure 5 could actually be representative for the vertical and horizontal plane patterns if either an unwanted or an intentional misalignment of the antenna's boresight direction with these planes were present. Non-zero cross-polarization fields in the vertical and horizontal planes can also be obtained for certain asymmetric antenna designs.

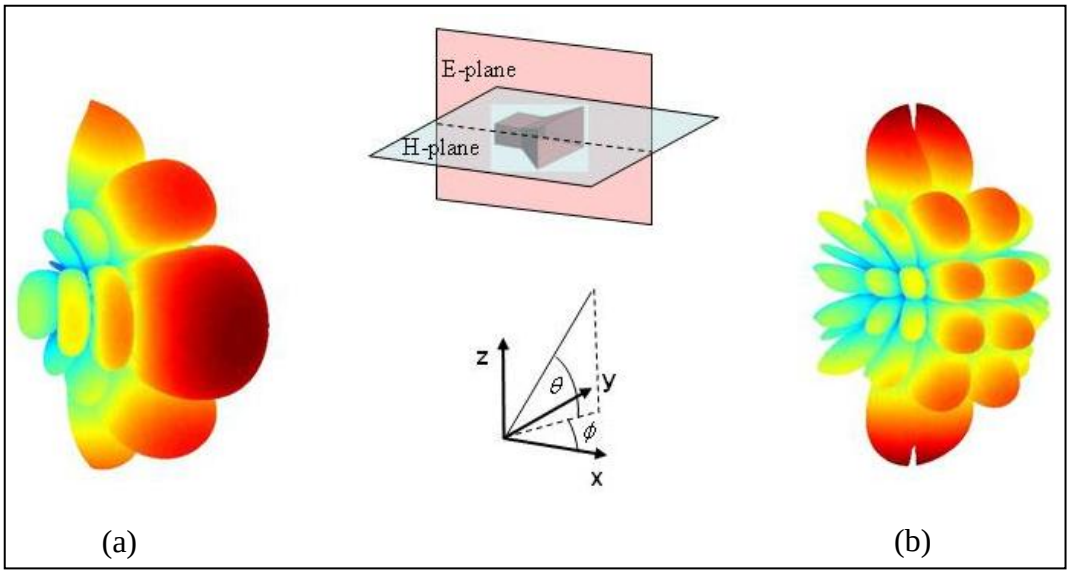

Figure 4. Three-dimensional representation of the far-field patterns radiated by a rectangular waveguide antenna at 4.5 GHz, showing: (a) co-polarization field magnitude; (b) cross-polarization field magnitude.

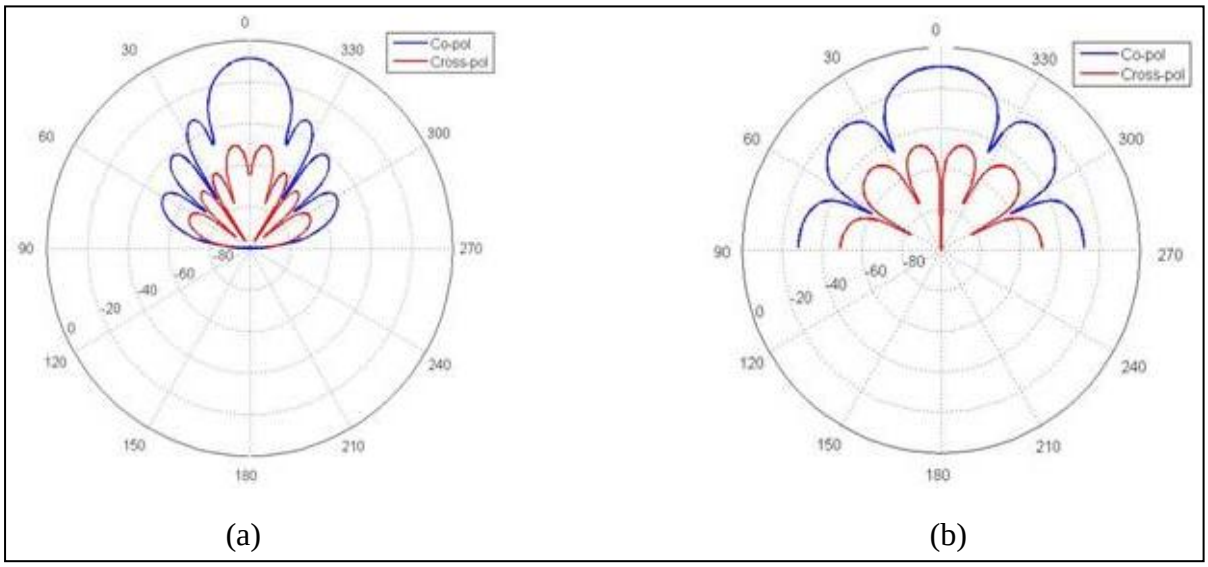

Figure 5. Two-dimensional, far-field patterns radiated by a rectangular waveguide antenna at 4.5 GHz, showing: (a) field magnitudes in the $\theta = 5^{o}$ plane; (b) field magnitudes in the $\phi = 5^{o}$ plane.

Note: The numbers shown as circle radii represent magnitude in dB.

2.5 Application to a Simple Polarimetric SAR Imaging Scenario

In this section we describe how to apply the approach developed in section 2.3 to the polarimetric strip-map SAR imaging scenario described in figure 6. The radar is assumed to be in the far-field with respect to the target and moves along a one-dimensional trajectory (aperture) in the horizontal plane. Furthermore, we assume that the radar configuration is monostatic and all antennas (transmitting and receiving, vertical, and horizontal) are collocated. The goal is to form a 2-D image of the target in the horizontal plane (although the target may be placed at any height with respect to this plane), for each polarization combination.

We assume that the target scattering data are obtained in the far-field through computer simulations, using plane-waves propagating at specific angles for both transmission and reception. To simplify our analysis, we consider no variation of the antenna patterns with the elevation angle. Therefore, in order to create an image in the horizontal plane, we only need the far-field target scattering data for propagation at $\theta = 0^{o}$ (remember, though, that in the vicinity of the target we still consider a full 3-D EM field model).

The algorithm for the SAR system simulation would involve the following steps:

- compute the polarimetric target signature under plane-wave transmission/reception (**SP** matrix) for all frequencies and azimuth angles of interest;
- obtain the transmitting and receiving antenna patterns in the horizontal plane (matrices $\mathbf{P}_T$ and $\mathbf{P}_R$), for the range of frequencies and angles of interest, either through computer

simulations or measurements (this must be performed for both vertically and horizontally polarized antennas);

- compute the **SA** matrix for each frequency and azimuth angle according to equation 19;
- convert the elements of the **SA** matrix from the frequency to the time domain via inverse Fourier transforms, after applying an appropriate spectral window;
- use equations (1) or (3) to form the SAR image via the BPA for each polarization combination.

Alternatively, the last two steps can be combined in one by applying the PFA; in that case, the SAR image is obtained directly by taking a 2-D inverse Fourier transform on the **SA** data.

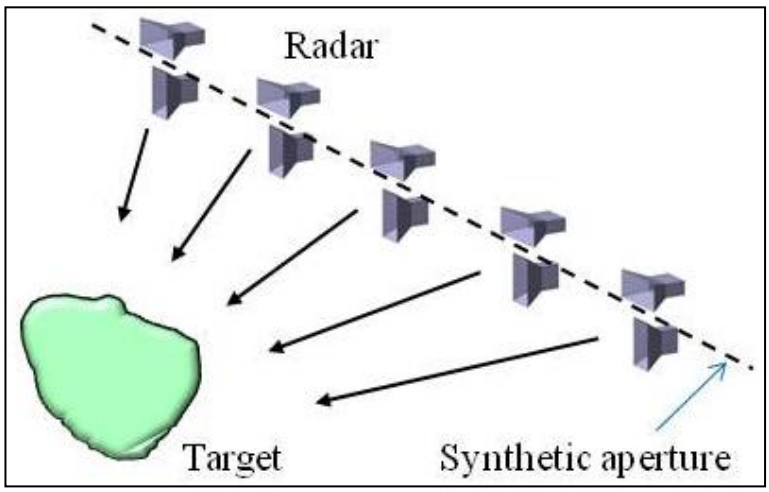

Figure 6. Schematic representation of a fully polarimetric two-dimensional SAR imaging system, operating monostatically in strip-map configuration.

In our previous modeling work on radar imaging systems (*11, 12*), the far-field SAR images have always been created from the elements of the **SP** matrix. In those models, the **SP** elements captured the entire angular variation of the EM scattering phenomena, while leaving the range dependence out (see equation 8). In our new approach, the SAR images are based on the elements of the **SA** matrix, which describe the angular dependence of both target scattering and antenna transmission/reception. The absolute values of the **SA** matrix elements are not relevant in interpreting the SAR images, where only the relative pixel intensity values are important. Moreover, the particular application considered in section 3 (detecting the presence of a weapon based on polarimetric image differences) requires taking the pixel intensity ratio of images created from different elements of the **SA** matrix. That case is obviously not affected by any extra normalization factors present in equation 19)

2.6 Limitations and Extensions of the Technique

The method of characterizing the performance of a fully polarimetric radar system we have outlined links together data specific to target scattering (the scattering matrix **SP**) with the antenna patterns (normalized effective lengths η) in order to obtain a modified version of the scattering matrix **SA** that captures the effect of both. It should be emphasized again that the technique applies in particular to low-frequency, strip-map SAR imaging systems, which typically use broad beam antennas and UWB waveforms. A spotlight SAR system normally uses only fields transmitted and received around the boresight direction, where typical radar antennas have very high polarization ratios. Therefore, for that case, the **SA** matrix closely resembles the **SP** matrix, and the analysis presented in the previous sections becomes irrelevant. The same can be said about a high-frequency SAR system (operating in the X-band or higher frequencies), in either strip-map or spotlight mode, which uses significantly smaller integration angles (*17*), typically around boresight.

In section 2.5, we presented a simple SAR imaging geometry that will be followed up with numerical examples in section 3. However, the technique does not have to be restricted to that particular scenario. Thus, we can easily extend it to a bistatic radar configuration, as outlined in section 2.1. Additionally, the transmitting/receiving and vertically/horizontally polarized antennas do not have to be identical or collocated. Although the configuration in figure 6 does not take into account the antenna patterns in elevation (it assumes they are constant), those could also be included in the model as long as they are coupled with the elements of the target **SP** matrix for the corresponding elevation angles. Notice that knowledge of the target signature variation with elevation, combined with 2-D synthetic aperture geometries, opens up the possibility to create 3-D images of the scene.

The configuration in figure 6 assumes that the aperture and the image are placed in the horizontal *x-y* plane and there is no physical ground plane present in the scene. That allows us to use the free-space antenna patterns and target signatures in deriving the polarimetric response of the radar system. A more realistic model would place the antennas at a specific height above an infinite ground plane. If the antenna is placed at a small height (less than a wavelength), then the changes in patterns produced by the ground plane need to be taken into account, together with the target signature changes produced by the same.

As already mentioned in section 2.6, this method cannot be applied to model a near-field scenario, since both the antenna patterns and the target signatures considered in equations 1–23 assume a far-field configuration. It is important to emphasize that the near-field antenna patterns, as well as the target signatures, may differ significantly from their far-field counterparts. The only way to correctly account for the near-field interactions between the radar antennas and the targets is to place them together in either a computer simulation or a measurement setup designed to evaluate the radar system performance. Currently, our ability to model a near-field scenario via computer simulations is limited by the fact that the AFDTD code operates only in

far-field configurations. Interestingly, another CEM code used in radar system simulation at ARL, Xpatch (*23*), offers a "near-field" modeling capability (*24*), which in effect closely resembles the technique outlined in this report (namely, combining far-field antenna patterns and target scattering, while the antennas are placed in the near-field of the targets). Given the inconsistencies between the two configurations, these models cannot be considered a rigorous representation of the near-field problem. Nevertheless, this approach can offer a reasonable approximation of the radar system operation in the near-field when other analysis methods are not available (*25*).

It is interesting to consider a formulation that reverses the process outlined in section 2.3. The method described so far (which we call the "forward problem") assumes that we know the matrices **SP** (polarimetric target signature) and **P** (polarimetric antenna patterns), and compute **SA** according to equation 19. In this approach, the goal is to predict the radar system performance in the presence of a known target. In many practical radar imaging applications, one needs to obtain a target characterization as accurate as possible based on measured data (the so-called "inverse problem"). The first step in this approach consists of the polarimetric radar calibration (*4–9*), in which one tries to derive the **P** matrices by measuring **SA** on a number of calibration targets, whose **SP** matrices are known. The second step involves finding the **SP** matrix of the unknown target of interest based on the **SA** matrix measured by the radar system, according to the following equation:

$$\mathbf{SP} = \left(\mathbf{P}_R^{\mathrm{T}}\right)^{-1} \mathbf{SA} \left(\mathbf{P}_T\right)^{-1}. \tag{25}$$

In practice, the calibration and compensation procedures involve more complex calculations than equation 25 suggests. Details on these techniques can be found in (*4–10*).

3. Numerical Results

3.1 Problem Definition and Methodology

In section 2, we formulated the theoretical approach to modeling the impact of the antenna patterns on the SAR images created by a polarimetric radar system. As a numerical application, we consider the weapon detection technique based on polarimetric radar image differences described in (*1*). In that report, we established that the ratio of the cross- to co-polarization image pixel intensities is significantly enhanced by the presence of a rifle (as compared to the case when the rifle is absent). That phenomenological finding enabled us to develop an algorithm that discriminates between the presence of an armed human and that of an unarmed human placed behind a wall, based on SAR images of the scene created for different polarization combinations. Importantly, the images presented in (*1*) were formed under the plane-wave assumption at transmission and reception (the **SP** matrix as described in section 2.3). In this new

study, we investigate the performance of the same algorithm when the images take into account the antenna patterns (the **SA** matrix).

The SAR imaging scenario was described in section 2.5, where we established the need to evaluate the plane-wave polarimetric radar response for various azimuth angles and frequencies, as well as the antenna patterns for the same sets of azimuth angles and frequencies. We obtained the former through AFDTD computer simulations, as described in (*1*). Notice that these were large-scale simulations, requiring the high-performance computing (HPC) systems available to us at the ARL Defense Supercomputing Resource Center (DSRC) in Aberdeen, MD (*26*).

The antenna patterns can be evaluated via analytic methods, computer simulations, or anechoic chamber measurements. In some simple cases, such as that presented in section 3.2, analytic expressions can provide good approximations to the antenna radiation pattern. For more complex antenna configurations, either computer simulations or measurements are required. Since complete measurement data were not available to us for the specific antennas considered in section 3.5, we used modeling data obtained with the FEKO software package (*27*). It is important to emphasize that the data provided by the FEKO models consist of the far-field radiated, complex electric field vertical and horizontal components, when the antenna is excited by a sinusoid with amplitude 1 V at its terminal, one frequency at a time (*28*). These field data are proportional to the antenna normalized effective lengths required by equation 18. As established in section 2.5, this type of data can be directly used in the SAR image formation process, without any additional normalization procedure.

Once the elements of the **SA** matrix are computed for all azimuth angles and frequencies, SAR images of the scene can be created for every polarization combination. In our application, we are only interested in the images based on SA_{VH} and SA_{VV}—more specifically, in the pixel-by-pixel ratio of those two images (*1*). By comparing the pixel ratio to a threshold, we decide whether the rifle is present or not in the scene.

The SAR images shown in the following sections are created with the Pioneer RCS software that implements the PFA algorithm. We employ a Hanning window in the frequency domain over the band of interest; however, unlike the images based on the **SP** matrix elements, where we used a Hanning window in the angular domain, as well, we leave the **SA** data unchanged with respect to angle, consistent with the formulation in section 2.1.

As suggested in section 2.3, we expect a radar system using antennas with low *PR* to exhibit decreased performance of the weapon detection scheme as compared to the idealized case analyzed in (*1*). In sections 3.2 through 3.4 we consider a set of simple, hypothetical antenna patterns that allow incremental changes to the PR_{RMS} parameter and evaluate the impact of these changes on the detection scheme performance. By finding the minimum PR_{RMS} value, where we notice no significant performance degradation as compared to the idealized case (based on **SP** matrix elements), we can make recommendations to the radar system designer in terms of

antenna cross-polarization suppression required by the polarimetric weapon detection scheme to work.

3.2 Example Involving Simple Antenna Patterns

In our first numerical example, we consider a set of hypothetical, simple antenna patterns, approximating the free-space, far-field radiation of an open rectangular waveguide operating in the TE_{10} (fundamental) mode, backed by an infinite metallic ground plane (*20*). We emphasize that these are not the exact patterns of such antenna, since they are based on the physical optics approximation of the equivalent currents along the antenna aperture (*20*). Moreover, this type of antenna is less frequently used in practical radar system implementations than, for instance, the horn antenna (*20*), which generally offers better sidelobe performance. Nevertheless, we use it in our analysis since the pattern equations can be written in closed form, and, at the same time, the general angular pattern variation is representative for a large number of radar antennas.

The open waveguide antenna geometry, for vertical and horizontal polarization, respectively, is shown in figures 7a and b, where the aperture coincides with the $x = 0$ plane. We use the same antenna geometry for the two polarizations, with the difference that in horizontal polarization the structure is rotated by 90º with respect to the x axis, as compared to vertical polarization. We also employ the same pairs of antennas for transmission and reception, in monostatic configuration. In the numerical calculations, we use $a = 0.3$ m, $b = 0.15$ m, which implies that the cutoff frequency of the TE_{10} mode is $f_c = 0.5$ GHz (*2*).

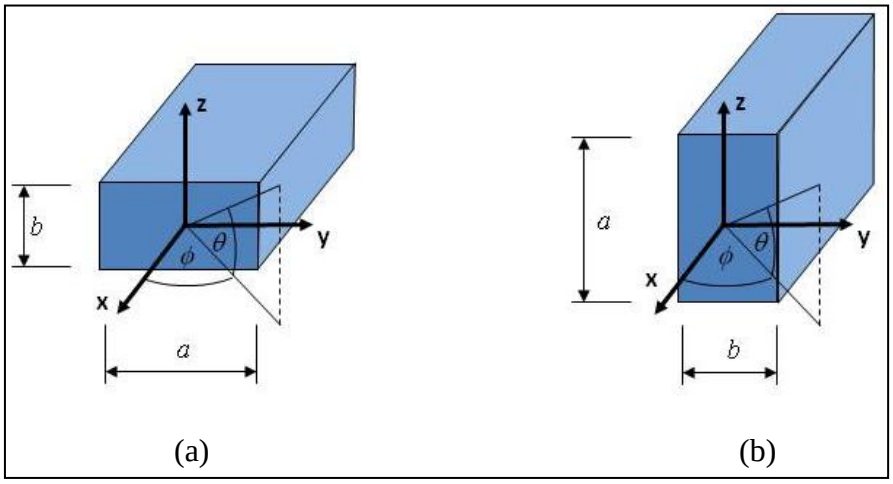

Figure 7. Geometry of the open rectangular waveguide antenna, showing: (a) vertical polarization and (b) horizontal polarization.

Note: The antenna is backed by an infinite metallic plane, which is not shown in the figure.

For vertical polarization, the components of the electric field radiated by the open rectangular waveguide antenna are approximated by (*20*):

$$E_V^V = \frac{j\pi abE_0 e^{-jkR}}{2\lambda R}\cos\phi \frac{\cos\frac{ka\sin\phi\cos\theta}{2}}{\left(\frac{ka\sin\phi\cos n\theta}{2}\right)^2 - \frac{\pi^2}{4}} \frac{\sin\frac{kb\sin\theta}{2}}{\frac{kb\sin\theta}{2}} \tag{26}$$

$$E_H^V = -\frac{j\pi abE_0 e^{-jkR}}{2\lambda R}\sin\theta\sin\phi \frac{\cos\frac{ka\sin\phi\cos\theta}{2}}{\left(\frac{ka\sin\phi\cos\theta}{2}\right)^2 - \frac{\pi^2}{4}} \frac{\sin\frac{kb\sin\theta}{2}}{\frac{kb\sin\theta}{2}}, \tag{27}$$

where E_0 is the maximum electric field amplitude propagating in the waveguide. Then, the components of the $\boldsymbol{\eta}$ vector can be written as:

$$\eta_V^V = A\frac{f}{f_c}\cos\phi \frac{\cos\frac{ka\sin\phi\cos\theta}{2}}{\left(\frac{ka\sin\phi\cos\theta}{2}\right)^2 - \frac{\pi^2}{4}} \frac{\sin\frac{kb\sin\theta}{2}}{\frac{kb\sin\theta}{2}} \tag{28}$$

$$\eta_H^V = -A\frac{f}{f_c}\sin\theta\sin\phi \frac{\cos\frac{ka\sin\phi\cos\theta}{2}}{\left(\frac{ka\sin\phi\cos\theta}{2}\right)^2 - \frac{\pi^2}{4}} \frac{\sin\frac{kb\sin\theta}{2}}{\frac{kb\sin\theta}{2}}, \tag{29}$$

where the constant A (with dimension meters) does not depend on range, angles, and frequency, and, as explained in section 2.5, is irrelevant for the SAR image interpretation. In a plane close to horizontal (θ close to 0º), we can approximate $\cos\theta \cong 1$ and $\sin\theta \cong 0$ and write:

$$\eta_V^V = A\frac{f}{f_c}\cos\phi \frac{\cos\frac{ka\sin\phi}{2}}{\left(\frac{ka\sin\phi}{2}\right)^2 - \frac{\pi^2}{4}} \tag{30}$$

$$\eta_H^V = -A\frac{f}{f_c}\sin\theta\sin\phi \frac{\cos\frac{ka\sin\phi}{2}}{\left(\frac{ka\sin\phi}{2}\right)^2 - \frac{\pi^2}{4}}, \tag{31}$$

where θ is fixed and ϕ is variable. Notice that the polarization ratio *PR* depends on the plane tilt angle θ, becoming infinity for $\theta = 0$º. Rather than allowing the tilt angle θ to determine the polarization ratio, we set PR_{RMS} to a specific value and employ the following equations:

$$\eta_V^V = \frac{\pi^2}{4}\frac{f}{f_c}\cos\phi\frac{\cos\frac{ka\sin\phi}{2}}{\left(\frac{ka\sin\phi}{2}\right)^2-\frac{\pi^2}{4}} \tag{32}$$

$$\eta_{H0}^V = -\frac{\pi^2}{4}\frac{f}{f_c}\sin\phi\frac{\cos\frac{ka\sin\phi}{2}}{\left(\frac{ka\sin\phi}{2}\right)^2-\frac{\pi^2}{4}} \tag{33}$$

$$\eta_H^V = \frac{\eta_{H0}^V\sqrt{\int_{\phi_1}^{\phi_2}\left|\eta_V^V(\phi)\right|^2 d\phi}}{PR_{RMS}\sqrt{\int_{\phi_1}^{\phi_2}\left|\eta_{H0}^V(\phi)\right|^2 d\phi}}. \tag{34}$$

Notice that we replaced the constant A by $\pi^2/4$ such that, at the cutoff frequency f_c, the maximum value of η_V^V is 1. Another aspect worth mentioning is that, by design, PR_{RMS} does not vary with frequency for this antenna (according to equation 34).

For the antenna in horizontal polarization, we can write similar expressions, as in equations 28 and 29, by swapping the ϕ and θ angles, as well as the vertical and horizontal components:

$$\eta_V^H = -A\frac{f}{f_c}\sin\theta\sin\phi\frac{\cos\frac{ka\sin\theta\cos\phi}{2}}{\left(\frac{ka\sin\theta\cos\phi}{2}\right)^2-\frac{\pi^2}{4}}\frac{\sin\frac{kb\sin\phi}{2}}{\frac{kb\sin\phi}{2}} \tag{35}$$

$$\eta_H^H = A\frac{f}{f_c}\cos\phi\frac{\cos\frac{ka\sin\theta\cos\phi}{2}}{\left(\frac{ka\sin\theta\cos\phi}{2}\right)^2-\frac{\pi^2}{4}}\frac{\sin\frac{kb\sin\phi}{2}}{\frac{kb\sin\phi}{2}} \tag{36}$$

Again, we are interested in evaluating these expressions in a plane close to horizontal (θ close to 0º), by using the following equations:

$$\eta_{V0}^H = -\frac{f}{f_c}\sin\phi\frac{\sin\frac{kb\sin\phi}{2}}{\frac{kb\sin\phi}{2}} \tag{37}$$

$$\eta_H^H = \frac{f}{f_c}\cos\phi \frac{\sin\frac{kb\sin\phi}{2}}{\frac{kb\sin\phi}{2}} \tag{38}$$

$$\eta_V^H = \frac{\eta_{V0}^H \sqrt{\int_{\phi_1}^{\phi_2} \left|\eta_H^H(\phi)\right|^2 d\phi}}{PR_{RMS}\sqrt{\int_{\phi_1}^{\phi_2} \left|\eta_{V0}^H(\phi)\right|^2 d\phi}}. \tag{39}$$

In these equations, PR_{RMS} is set to a specific value (same as for the vertically polarized antenna) and the patterns are normalized such that, at the cutoff frequency f_c, the maximum value of η_H^H is 1 (this is consistent with the maximum value of η_V^V, since the two must coincide in the boresight direction of the vertical and horizontal antennas).

3.3 Imaging of a Human in a Simple Room

We apply the antenna patterns developed in the previous section to the relatively simple scenario of a human placed in the middle of a four-wall room. The geometry is described in figure 8. The room dimensions are 5 m × 3.5 m × 2.2 m (197 in × 138 in × 87 in), with walls made of brick (ε_r = 3.8, σ = 0.03 S/m, thickness 20 cm). The ceiling and floor are represented as 15-cm-thick concrete slabs, with ε_r = 6.8, σ = 0.1 S/m. The human is represented by the "fit man" model described in (*29*). In the case when he holds an AK-47 rifle, this has a tilt angle of 45º (*1*). The AFDTD grid has a cell size of 5 mm and is comprised of approximately 400 million cells. In order to obtain a SAR image, we compute the radar response for angles between –30º and 30º azimuth, in 0.5º increments, and frequencies between 0.5 and 3.5 GHz, in 13.3 MHz increments. (Notice that, in practice, this antenna could not be used over such a wide frequency band without generating higher waveguide propagation modes (*2*); for the particular aperture dimensions that we chose in this example, the TE_{01} and TE_{20} modes would start to be generated over 1 GHz). Taking into account the windowing procedure, the approximate image resolutions are 10 cm in down-range and 14 cm in cross-range. The simulations were run on the Harold system at ARL DSRC (*26*), using 24 cores per angle, for a total of about 25,000 CPU hours per image.

In figures 9 through 11 we present the SAR images of the human in the simple room, with and without the rifle, for various levels of PR_{RMS}. The images represent top-view, 2-D pseudo-color maps, with downrange on the *x*-axis and cross-range on the *y*-axis. In all images, the human faces left, while the radar looks from the left side. The intensity scales are always in dB. For each level of PR_{RMS}, we display the images obtained for vertical-vertical (V-V) and horizontal-vertical (H-V) polarizations and mark the highest intensity pixel dB value around the human location in each case. The key measure for the ability to discriminate between the cases where the human is

armed or unarmed is the ratio (difference in dB) between the cross-polarization (H-V) and co-polarization (V-V) pixel intensities.

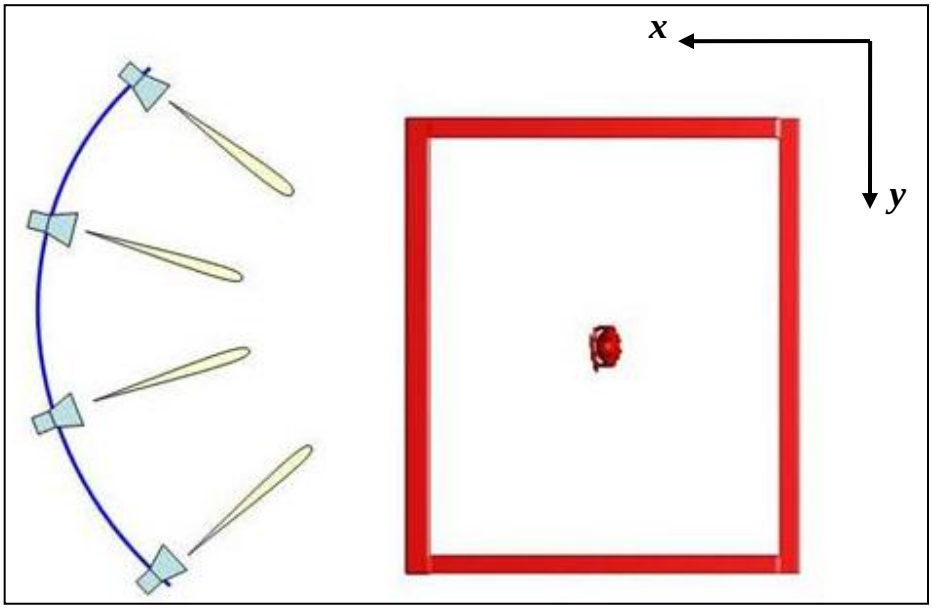

Figure 8. Top view of the simple four-wall room with a human carrying an AK-47 rifle and placed in the middle of the room, showing a schematic representation of the synthetic radar aperture on the left side.

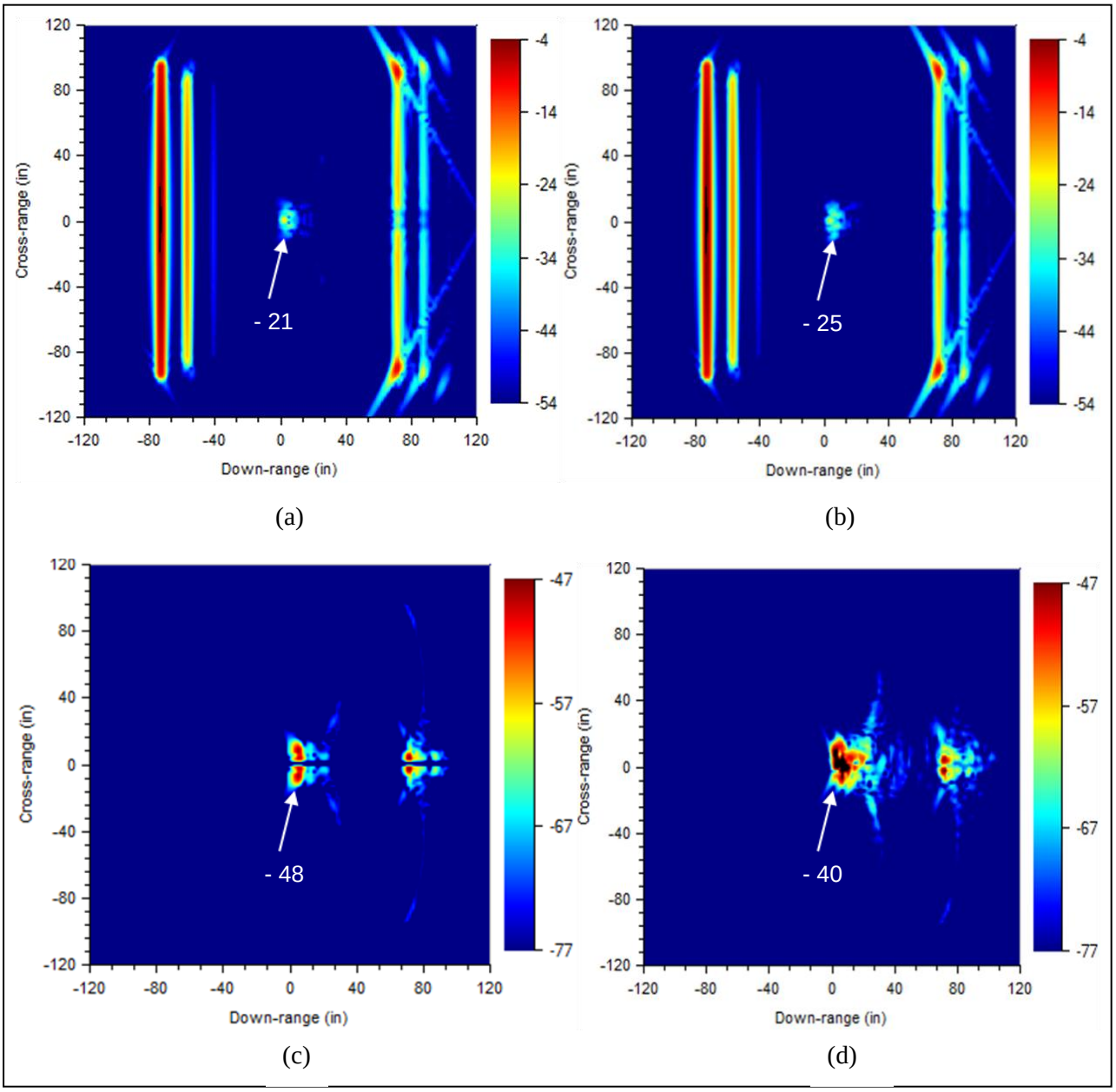

Figure 9. SAR images of the human placed in a middle of a brick wall room, under the plane wave assumption, showing: (a) V-V polarization, human unarmed; (b) V-V polarization, human with AK-47; (c) H-V polarization, human unarmed; and (d) H-V polarization, human with AK-47.

Note: All the numerical values indicated inside the images are in dB.

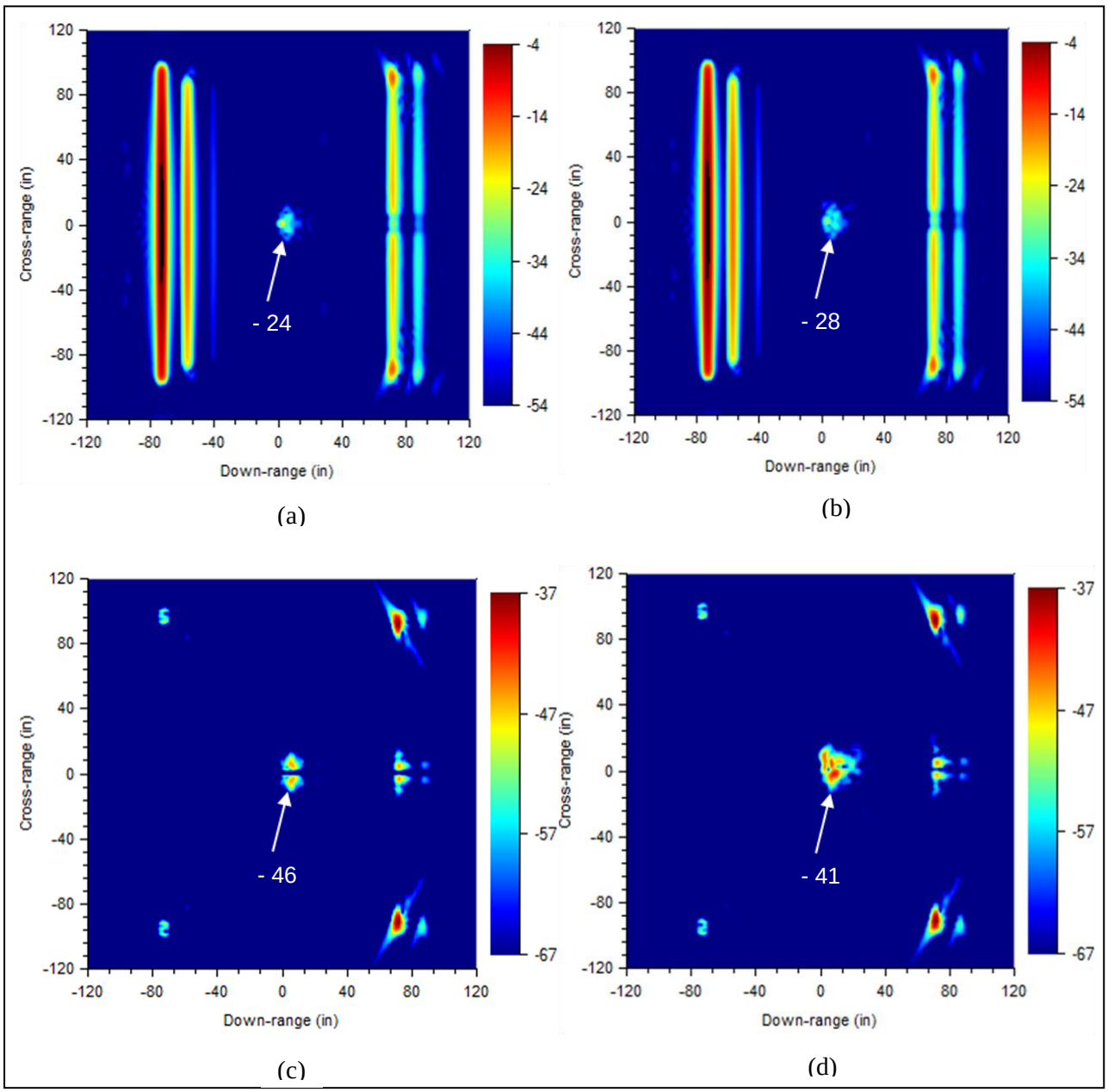

Figure 10. SAR images of the human placed in a middle of a brick wall room, including the effects of open waveguide antennas with PR_{RMS} = 20 dB, showing: (a) V-V polarization, human unarmed; (b) V-V polarization, human with AK-47; (c) H-V polarization, human unarmed; and (d) H-V polarization, human with AK-47.

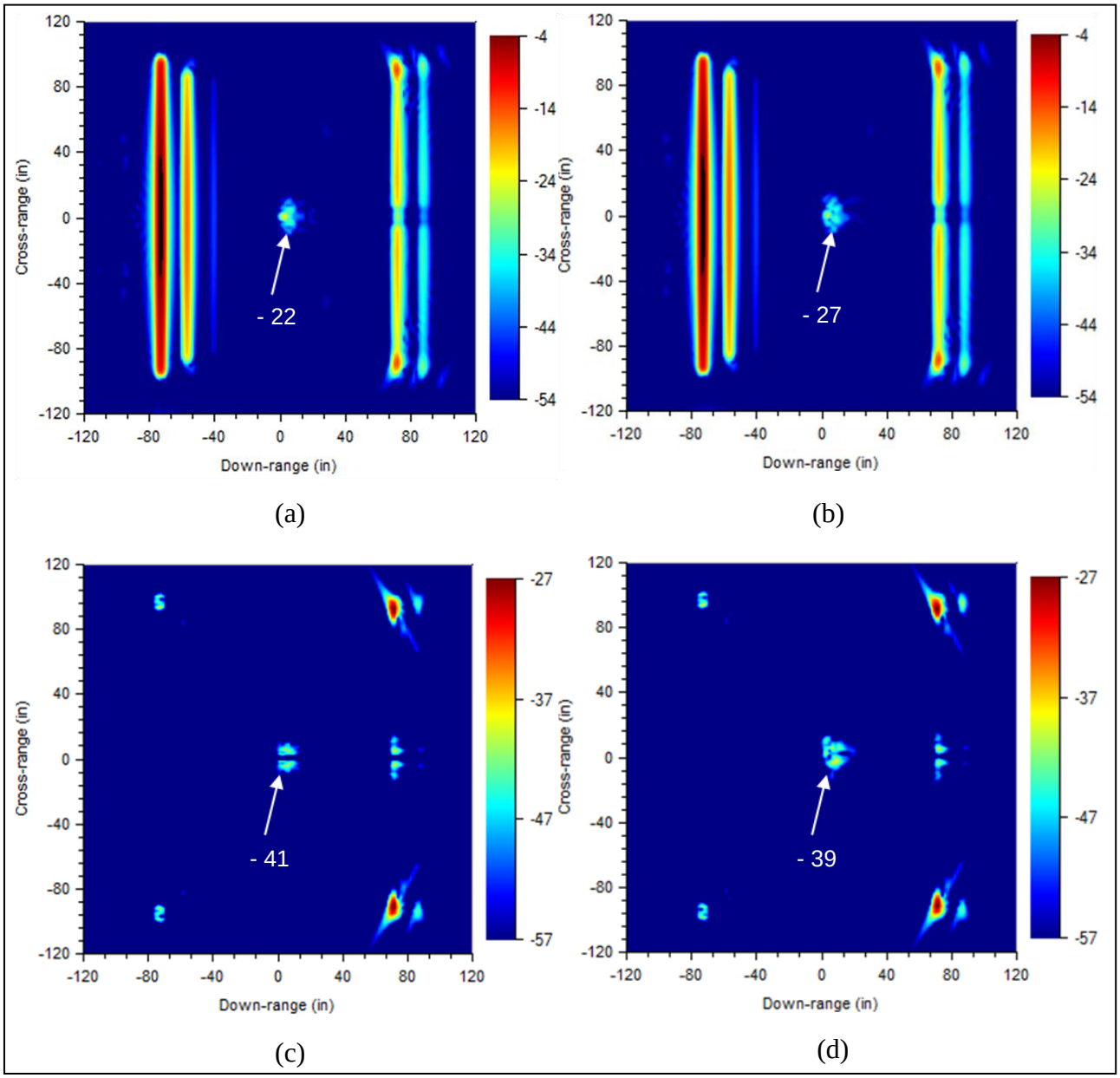

Figure 11. SAR images of the human placed in a middle of a brick wall room, including the effects of open waveguide antennas with PR_{RMS} = 10 dB, showing: (a) V-V polarization, human unarmed; (b) V-V polarization, human with AK-47; (c) H-V polarization, human unarmed; and (d) H-V polarization, human with AK-47.

We start with the plane-wave model of the SAR imaging system, when PR_{RMS} is infinity, in figure 9. This case is identical to the one analyzed in reference (*1*). It shows a significant gain (12 dB) in the cross-to-co-polarization ratio when the rifle is present. Figure 10 takes into account the polarimetric antenna patterns with PR_{RMS} = 20 dB. The cross-to-co-polarization ratio rifle gain drops to about 9 dB in this scenario. Interestingly, we notice some significant changes in the cross-polarization SAR images, particularly the presence of the room corners, which were absent from the images in figures 9c and 9d. This is the effect of coupling various elements of

the **SP** matrix through the antenna patterns, as explained in section 3.3. Figure 11 shows the images obtained for PR_{RMS} = 10 dB, where we notice a further drop in the cross-to-co-polarization ratio rifle gain down to 7 dB. Table 1 summarizes the relationship between the PR_{RMS} and the cross-to-co-polarization ratio gain for PR_{RMS} ranging from infinity to 0 dB. As expected, the trend demonstrates that a lower PR_{RMS} level leads to less difference between the images of the armed and unarmed human. The impact of the antenna effect on the rifle detection scheme based on this difference is examined in section 3.4, where we consider a more complex scenario.

Table 1. Comparison of maximum pixel intensity in the human areas within the SAR images presented in sections 3.2 and 3.3, in co- and cross-polarization, for the cases with and without rifle (all values in dB).

Note: co-polarization denotes the V-V case, whereas cross-polarization denotes the H-V case.

Antenna type	PR_{RMS} (dB) or tilt angle	Cross-to-co-pol ratio, no rifle (dB)	Cross-to-co-pol ratio, with rifle (dB)	Gain in ratio with rifle (dB)
Open waveguide	Infinity	–27	–15	12
	30	–23	–13	10
	20	–22	–13	9
	10	–19	–12	7
	0	–17	–12	5
SIRE (TEM-horn and Vivaldi)	1º	–20	–9	11
	2º	–14	–7	7

3.4 Application to Imaging of a Complex Room

A model of higher complexity is shown in figure 12, where four humans (each represented by the “fit man” model) are placed in a complex room of dimensions 10 m × 7 m × 2.2 m (197 in × 138 in × 87 in). The room contains furniture and interior walls made of sheetrock. The 20-cm-thick outer walls are made of brick and are equipped with doors and windows. A detailed

description of the scene, as well as the dielectric properties of the materials, is given in (*12*). The AFDTD grid contains about 1.68 billion cells with 5 mm size. The SAR images are obtained with an aperture placed on the left side of the page, with angles between –30º and 30º, in 0.25º increments. The frequency varies between 0.5 and 2.5 GHz, in 6.67 MHz increments. The image resolutions are 15 cm in down-range and 20 cm in cross-range. The simulations were again run on the Harold system, using 64 cores per angle, for a total of 100,000 CPU hours per image.

Figures 13 through 15 show the SAR images obtained for H-V polarizations, in the cases unarmed vs. armed (the humans are either all unarmed or all armed) and various levels of the PR_{RMS} parameter. Qualitatively, we notice the same effects of decreasing PR_{RMS}, as in the images presented in section 3.3. For this scenario, the antenna coupling (figures 14 and 15) makes a large number of vertical corners apparent in the cross-polarization images, including the corners formed by the windows and doors with the walls.

A detection scheme that decides whether the humans are armed or unarmed was presented in (*1*). We apply the same scheme to the scenario considered in this section, for various PR_{RMS} levels. Thus, we reduce the image resolution by means of a square moving average filter with size 15-by-15 pixels in the original SAR images. Then, we eliminate all the "noise" pixels, with intensities below a certain threshold (–40 dB for V-V images and –60 dB for H-V images). Finally, we form the cross-to-co-polarization ratio of the remaining pixel intensities and compare them to a threshold. In general, we increase the detection threshold until we observe no false alarms (meaning there are no positive detections for the case when the humans do not carry rifles). The final detection maps are shown in figures 16 and 17. For the case shown in figure 16a, PR_{RMS} = 30 dB, and all the rifle carriers are detected. In figure 16b, we consider PR_{RMS} = 20 dB and notice that only three out of the four humans carrying rifles are detected. Figure 17 shows that the detection scheme breaks down for PR_{RMS} = 10 dB, in the sense that we obtain numerous false alarms and missed detections. In particular, all the false alarms are created by room corners, which, as seen in figure 15, start to show prominently in the cross-polarization images. For relatively low PR_{RMS}, the cross-to-co-polarization ratios of these image features become larger than those of the humans with rifles, leading to the failure of the discrimination algorithm presented above. Notice that varying the detection threshold up or down does not help in this case: if the threshold is increased, we miss detecting the rifle carriers, whereas if it is decreased we include too many unwanted features as positive detections. The detection threshold values used for the cases shown in figures 16 and 17 are listed in table 2.

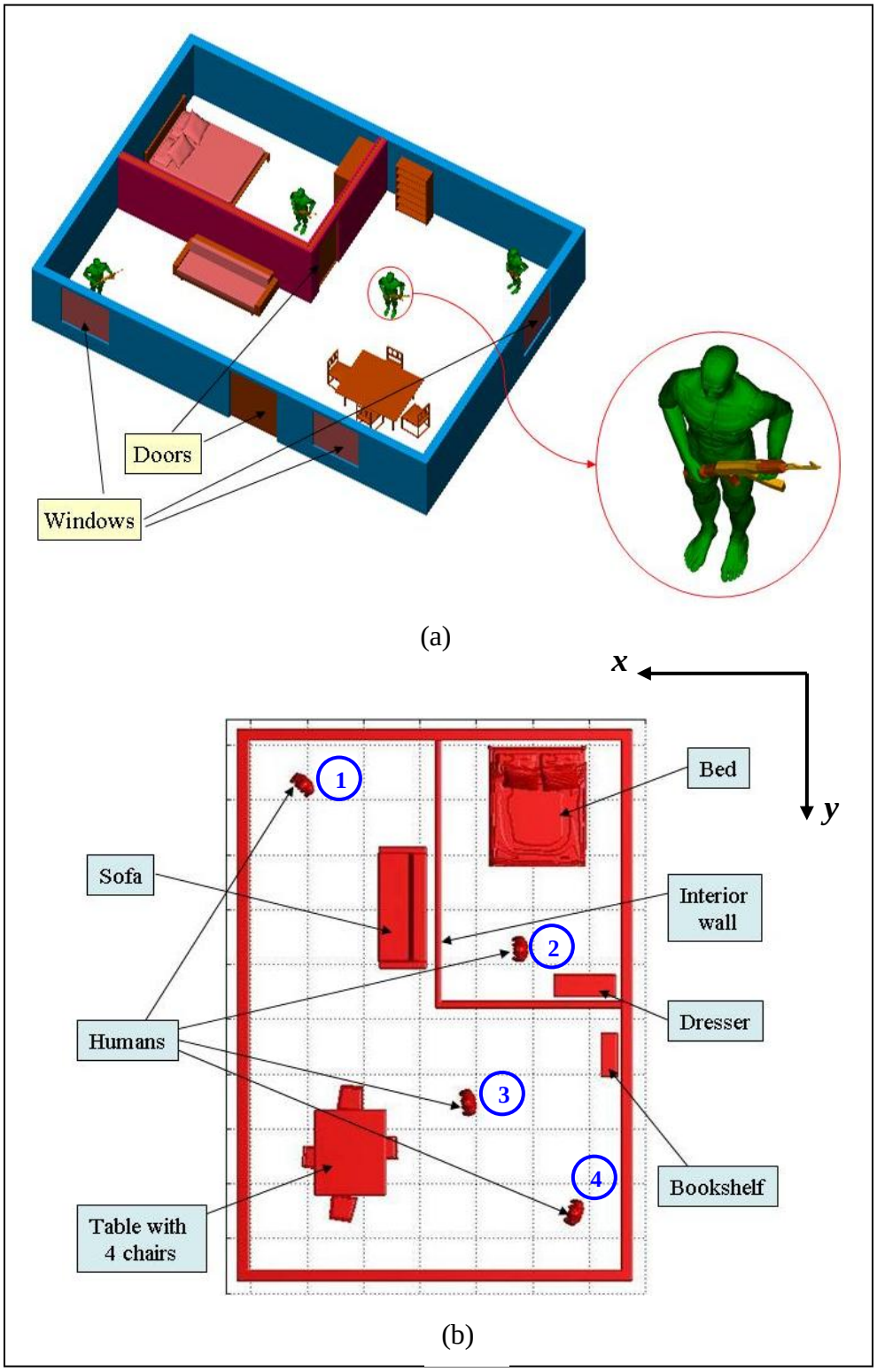

Figure 12. The complex room containing humans and furniture objects showing (a) perspective view (humans carrying rifles) and (b) top view (humans unarmed).

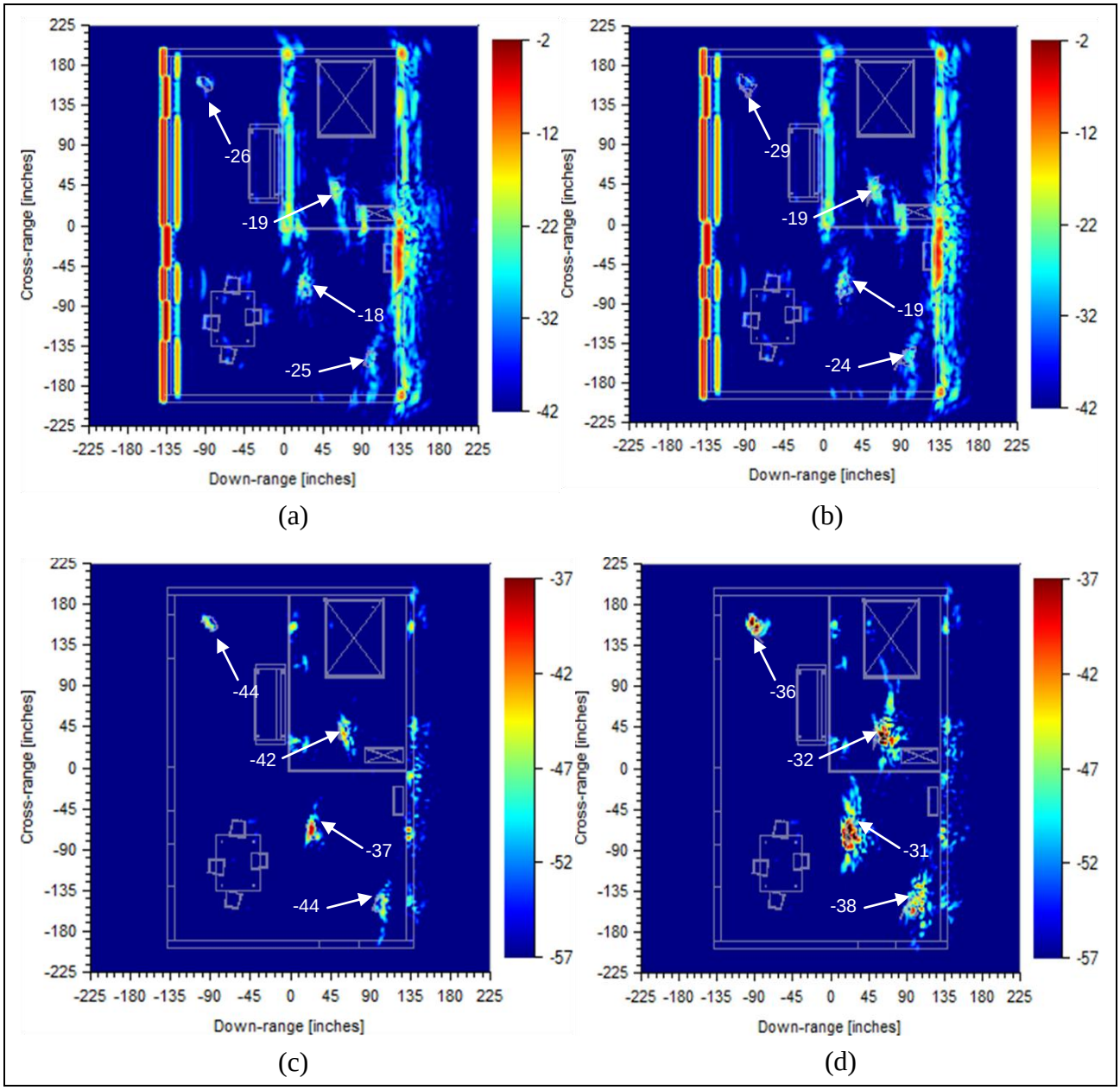

Figure 13. SAR images of the complex room under the plane wave assumption showing: (a) V-V polarization, all humans unarmed; (b) V-V polarization, all humans with AK-47; (c) H-V polarization, all humans unarmed; and (d) H-V polarization, all humans with AK-47.

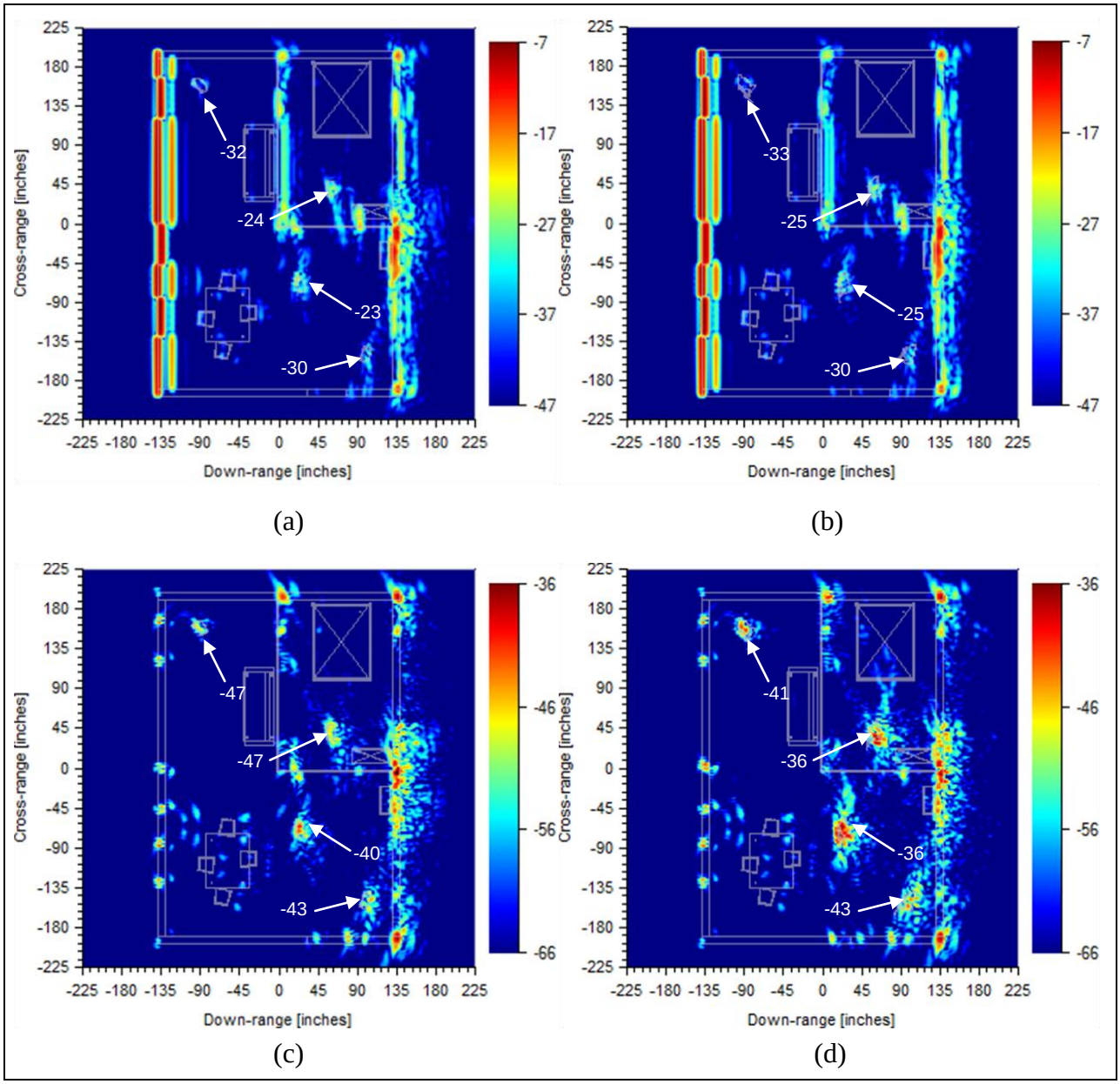

Figure 14. SAR images of the complex room that include the effects of open waveguide antennas with PR_{RMS} = 20 dB showing: (a) V-V polarization, all humans unarmed; (b) V-V polarization, all humans with AK-47; (c) H-V polarization, all humans unarmed; and (d) H-V polarization, all humans with AK-47.

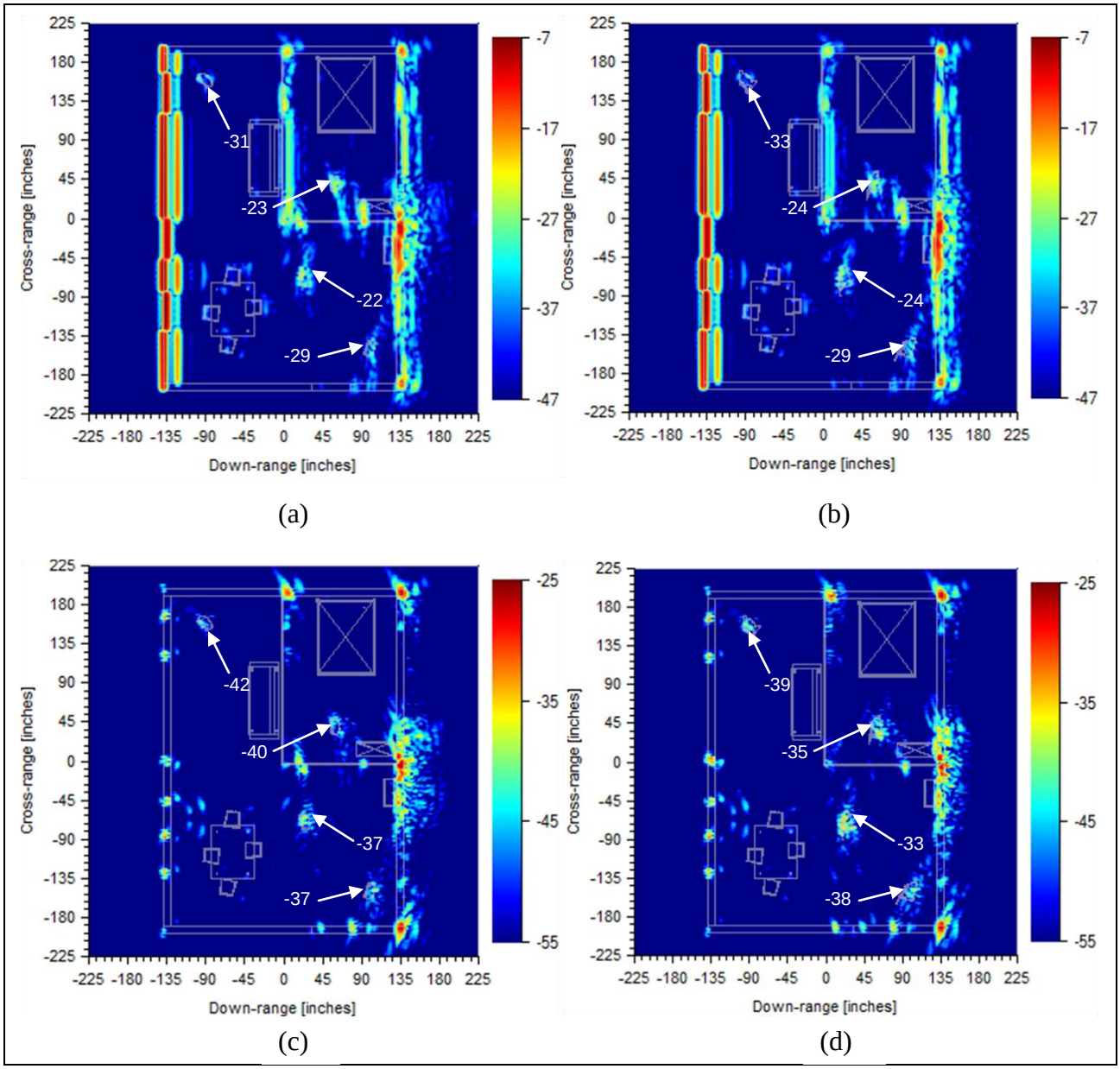

Figure 15. SAR images of the complex room that include the effects of open waveguide antennas with PR_{RMS} = 10 dB showing: (a) V-V polarization, all humans unarmed; (b) V-V polarization, all humans with AK-47; (c) H-V polarization, all humans unarmed; and (d) H-V polarization, all humans with AK-47.

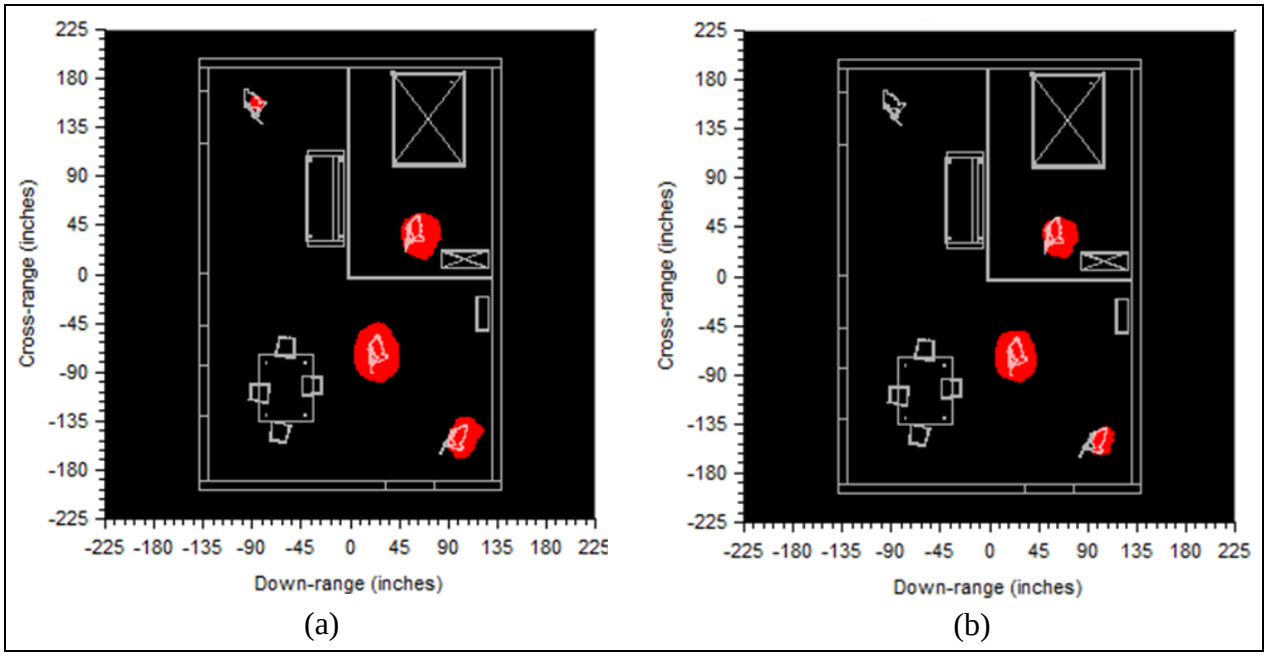

Figure 16. Detection maps for the complex room shown in figure 12, for a SAR system equipped with open waveguide antennas with (a) PR_{RMS} = 30 dB and (b) PR_{RMS} = 20 dB.

Notes: In the scenario shown here, all the humans carry AK-47 rifles. The red spots indicate positive detections.

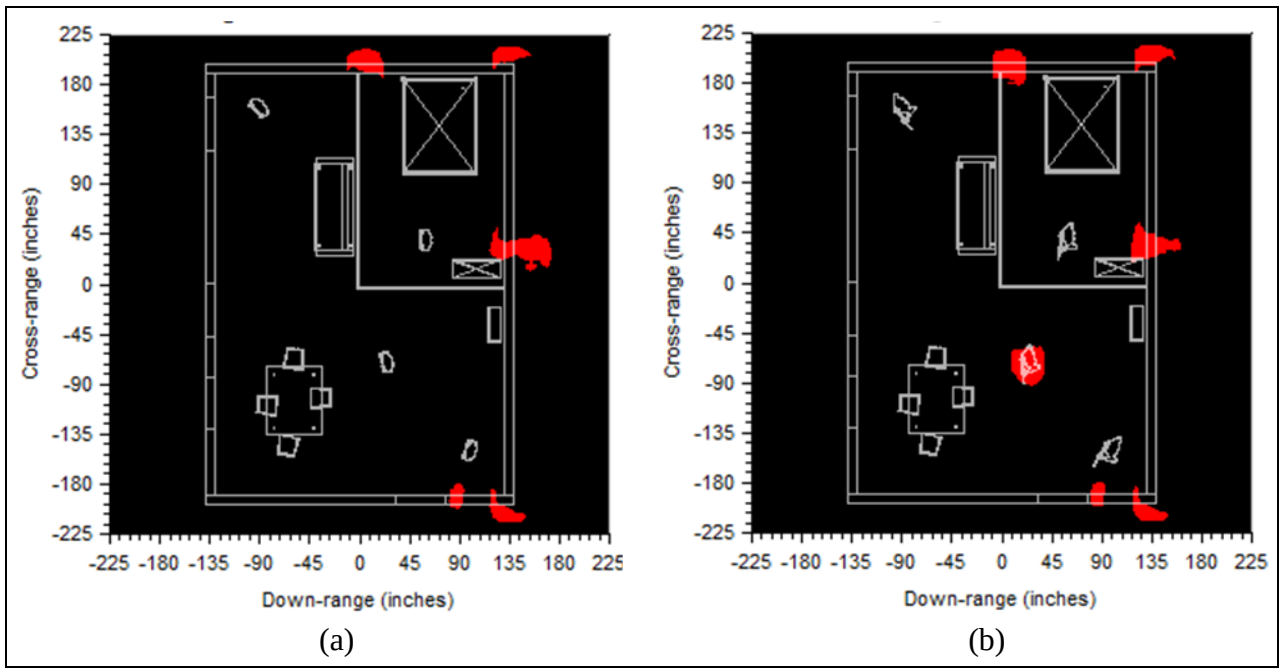

Figure 17. Detection maps for the complex room in figure 12, for a SAR system equipped with open waveguide antennas with PR_{RMS} = 10 dB, showing the cases where (a) all humans are unarmed and (b) all humans carry AK-47 rifles.

Table 2. Detection threshold for the weapon discrimination scheme described in sections 3.4 and 3.5, for various antenna systems and cross-polarization properties.

Antenna type	Open waveguide				SIRE (TEM-horn and Vivaldi)		
Cross-polarization metric	PR_{RMS} (dB)	30	20	10	Tilt angle	1º	2º
Detection threshold (dB)		–17	–15	–11		–13	–10

Based on the examples shown in this and the previous sections, we draw the broad conclusion that antennas with good cross-polarization suppression (of at least 20 dB, but preferably 30 dB, as measured by PR_{RMS}) are required in order to successfully employ the cross-to-co-polarization ratio in the rifle discrimination technique. Obviously, these numbers are not universally valid for all possible scenarios, but depend on the weapon type and orientation, the human body size, shape, and orientation, as well as other clutter objects present in the room. It seems that the human placed in the upper left corner of the complex room images is more difficult to detect when the cross-polarization antenna patterns are taken into account (interestingly, that human is rotated by the largest angle in azimuth, namely, 45º with respect to broadside). This result hints to a more subtle relationship between target orientation, shape of the antenna pattern, and integration angle used by the SAR image formation algorithm. Moreover, these results may change if one considers other frequency bands.

Nevertheless, the figure of about 25 dB for the antenna cross-polarization suppression gives a rough guideline to the radar engineer designing an UWB, wide-beam, SAR imaging system that attempts to detect targets based on polarimetric differences. Interestingly, our results are consistent with the findings in (*10*), where 30 dB of cross-polarization isolation are recommended for a polarimetric SAR application at C-band. Additionally, the method outlined in this study allows the analysis of a specific radar antenna design in order to predict the performance of the polarimetric target detection scheme for that radar system and scenario, as shown in the following section.

3.5 Examples Involving the SIRE Radar Antennas

In this section we apply the technique developed in section 2 to a set of more realistic antenna pattern data: the transmitting and receiving antennas of the synchronous impulse reconstruction (SIRE) radar (*30*). The transmitting antenna, shown in figure 18a, is a transversal electromagnetic (TEM) horn (*31*), while at the receiving side the radar uses a Vivaldi notch antenna (*22*), shown in figure 18b. Both are UWB antennas, designed to work in the frequency

range of the SIRE radar (0.5 to 2.5 GHz). In the forward-looking configuration, the SIRE radar antenna assembly is made of multiple TEM-horn and Vivaldi elements (*30*). However, for our STTW imaging application, we assume that the radar is configured in the side-looking, strip-map SAR mode (*3*) and only one set of vertically and horizontally polarized antennas is employed for both transmission and reception. Moreover, we assume that all the antennas are collocated for one radar position along the synthetic aperture, in effect creating a monostatic configuration.

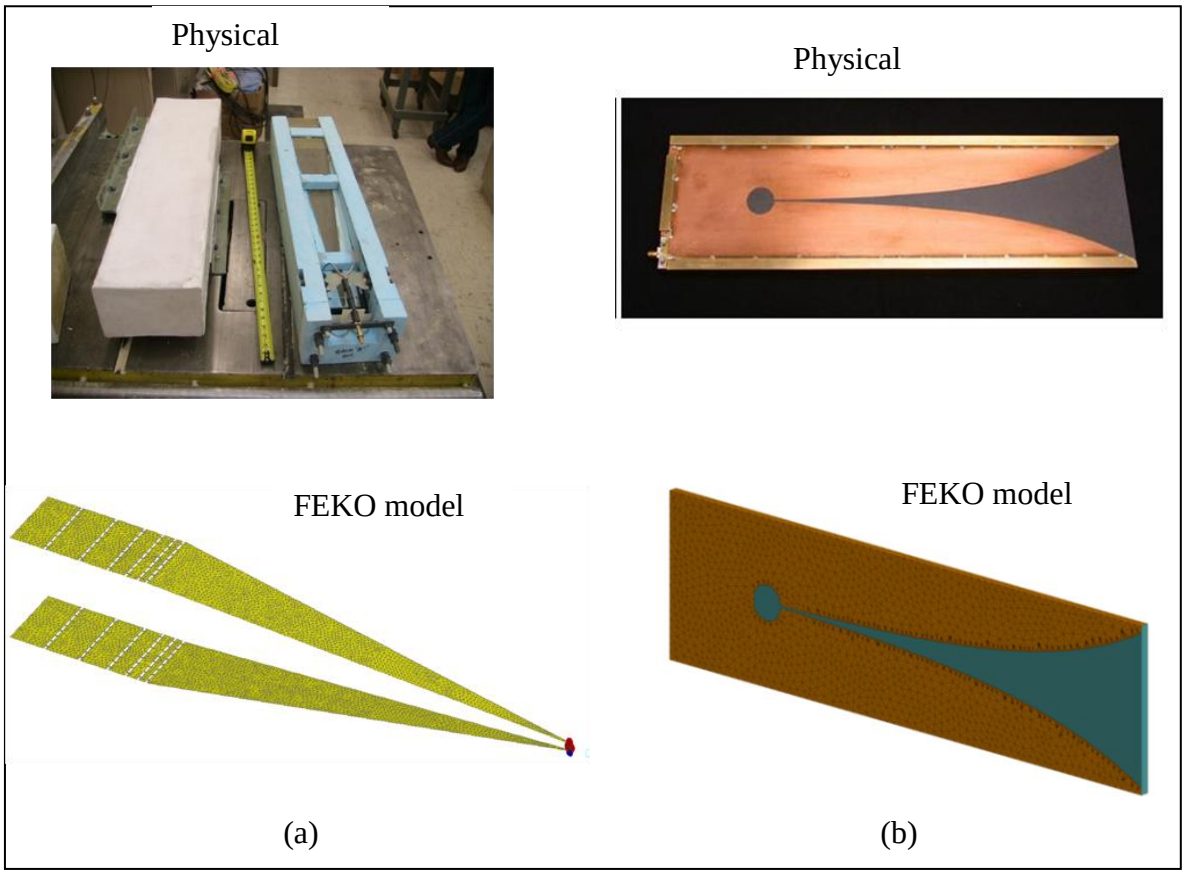

Figure 18. The SIRE radar antennas for the (a) transmitter and (b) receiver, showing pictures of the physical antennas as well as wire-frame meshes used in FEKO simulations.

Note: In this figure, both antennas are configured for vertical polarization.

As explained in section 3.1, the patterns of the SIRE transmitting and receiving antennas were obtained via FEKO simulations, based on detailed models of the two antenna geometries, for all the angles and frequencies of interest. However, further processing of the FEKO output data was performed for our application, in order to mitigate possible SAR image artifacts that may arise when the antennas are excited with UWB pulses. (Notice that we were not able to include all the details of the antenna design in the FEKO models, particularly the areas around the feeding points, which are crucial in determining important parameters such as the input impedance and S_{11} [*20*]). Thus, instead of using complex numbers to represent the normalized effective lengths of the antenna, as provided in the FEKO output files, we considered only the magnitude of these

numbers, effectively ensuring that the phase center of the antenna does not change its spatial position with frequency or propagation angle (this eliminates any issue related to excitation pulse dispersion).

Another modification to the FEKO output data consists of smoothing out the variation of the η parameters with respect to frequency, in order to eliminate any late-time replicas of the excitation pulse that would appear as unwanted echoes in the SAR images (see figure 19). We emphasize that the changes in the simulated antenna pattern data are meant only to improve the antenna impulse response and should not significantly impact its polarimetric characteristics.

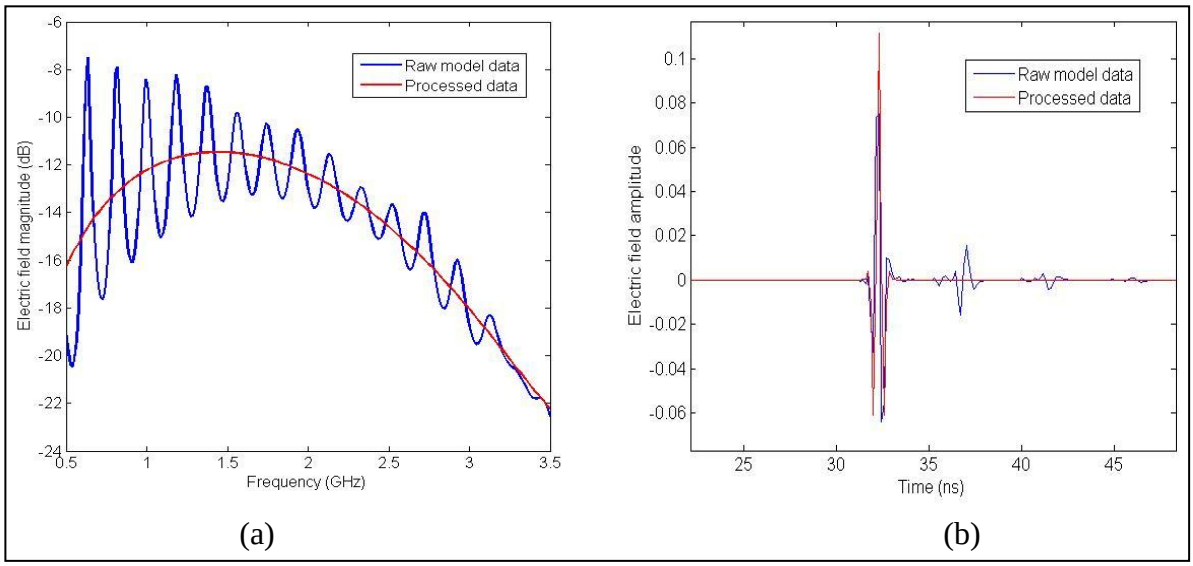

Figure 19. The vertical electric field magnitude for the SIRE transmission antenna at $\phi = 0^o$ and $\theta = 1^o$, before and after the smoothing procedure, shown here in: (a) frequency domain; (b) time domain.

Notes: The original data were obtained via FEKO simulation. The smoothing consists of a cubic polynomial fit. The time-domain version was obtained via inverse Fourier transform after applying a Hanning window.

The antennas are assumed to have an elevation tilt of 1º or 2º (again, we avoid considering perfectly symmetric antennas with no elevation tilt, which would theoretically lead to an infinite polarization ratio). After the processing steps previously described, we obtained the following PR_{RMS}, at 2 GHz (the center of the pulse spectrum), in the horizontal ($\theta = 0^o$) plane:

- for the transmitting antenna with 1º tilt, 21 dB in vertical polarization and 25 dB in horizontal polarization;
- for the transmitting antenna with 2º tilt, 15 dB in vertical polarization and 19 dB in horizontal polarization;
- for the receiving antenna with 1º tilt, 34 dB in vertical polarization and 36 dB in horizontal polarization;

- for the receiving antenna with 2º tilt, 28 dB in vertical polarization and 30 dB in horizontal polarization.

The transmitting and receiving antenna patterns in the horizontal plane for 2º tilt, in both polarizations, within the angular span of interest (–30 º to 30 º), at 2 GHz are shown in figure 20. It should be noted that, qualitatively, these patterns are very similar to those of the open waveguide antenna described in section 3.2. A significant difference is displayed by the transmitting antenna in horizontal polarization, for which the fields radiated around ±25º exceed those radiated at broadside (0º), for co-polarization. Other aspects worth mentioning with regard to the SIRE antennas are the fact that the TEM horn (transmitting) antenna has generally poorer polarization ratios than the Vivaldi (receiving) antenna, while the horizontal polarization displays larger PR_{RMS} than the vertical polarization (in the horizontal plane).

Both scenarios described in section 3.3 and 3.4 were re-analyzed using the SIRE radar antenna pattern data. Figure 21 shows the SAR images obtained in the simple room case, for V-V and H-V polarizations, when the human is armed or unarmed and both SIRE antennas are tilted by 2º. In this case, the gain in the cross-to-co-polarization ratio when the rifle is present is 7 dB. If the elevation tilt were set to 1º, we would obtain a cross-to-co-polarization gain of 11 dB (a summary of these performance metrics can be found in table 1).

In figure 22, we display the H-V SAR images of the complex room when all the humans are armed, for 1º and 2º antenna elevation tilt, respectively. As expected, these images are similar to those obtained for the corresponding scenarios in figures 13 and 14. The detection maps obtained for those two cases via the procedure outline in section 3.4 are shown in figure 23. For an elevation tilt of 1º, all four targets are correctly detected. However, for an elevation tilt of 2º, only three out of four targets are detected. The detection thresholds used for these scenarios are listed in table 2. Notice that these results are consistent with those obtained in section 3.4, showing that polarization ratios of at least 20 dB (preferably 30 dB) are required for the radar antennas in order to achieve good weapon detection performance of the polarimetric technique outlined in this report.

We should also mention that the scenarios included in this section are somewhat artificial, in the sense that we needed to introduce a small elevation tilt to the antennas in order to illustrate the method. However, as a general conclusion we can clearly state that the Vivaldi antenna has much better cross-polarization suppression than the TEM horn antenna, exceeding the strong requirement of 30 dB polarization ratio for small tilt angles. On the other hand, the TEM horn antenna displays marginal cross-polarization properties, with the largest performance degradation coming from the vertical polarization configuration.

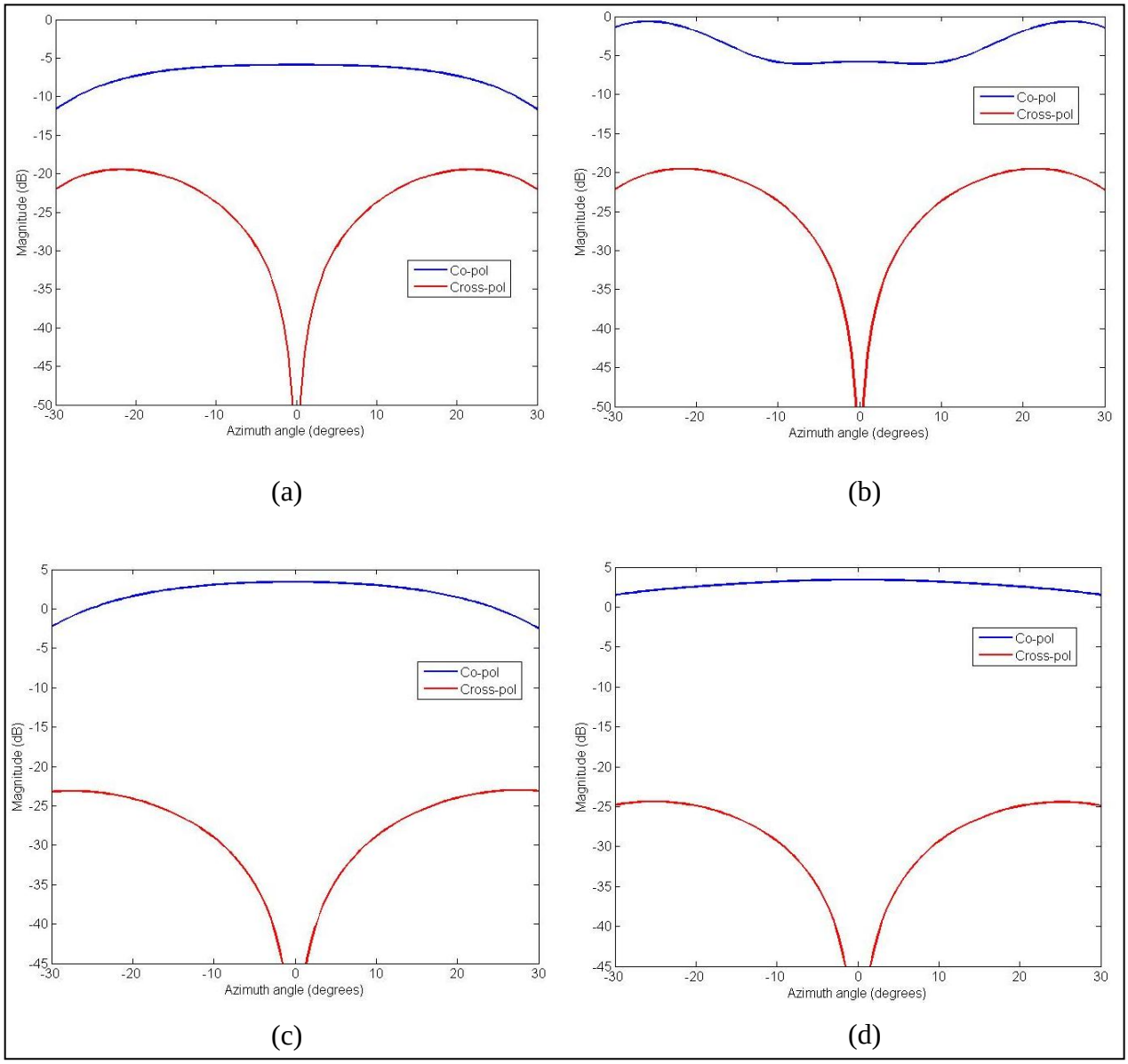

Figure 20. SIRE antenna patterns in the horizontal plane, at 2 GHz, with antennas at 2º elevation tilt, showing: (a) transmitting antenna in vertical polarization; (b) transmitting antenna in horizontal polarization; (c) receiving antenna in vertical polarization and (d) receiving antenna in horizontal polarization.

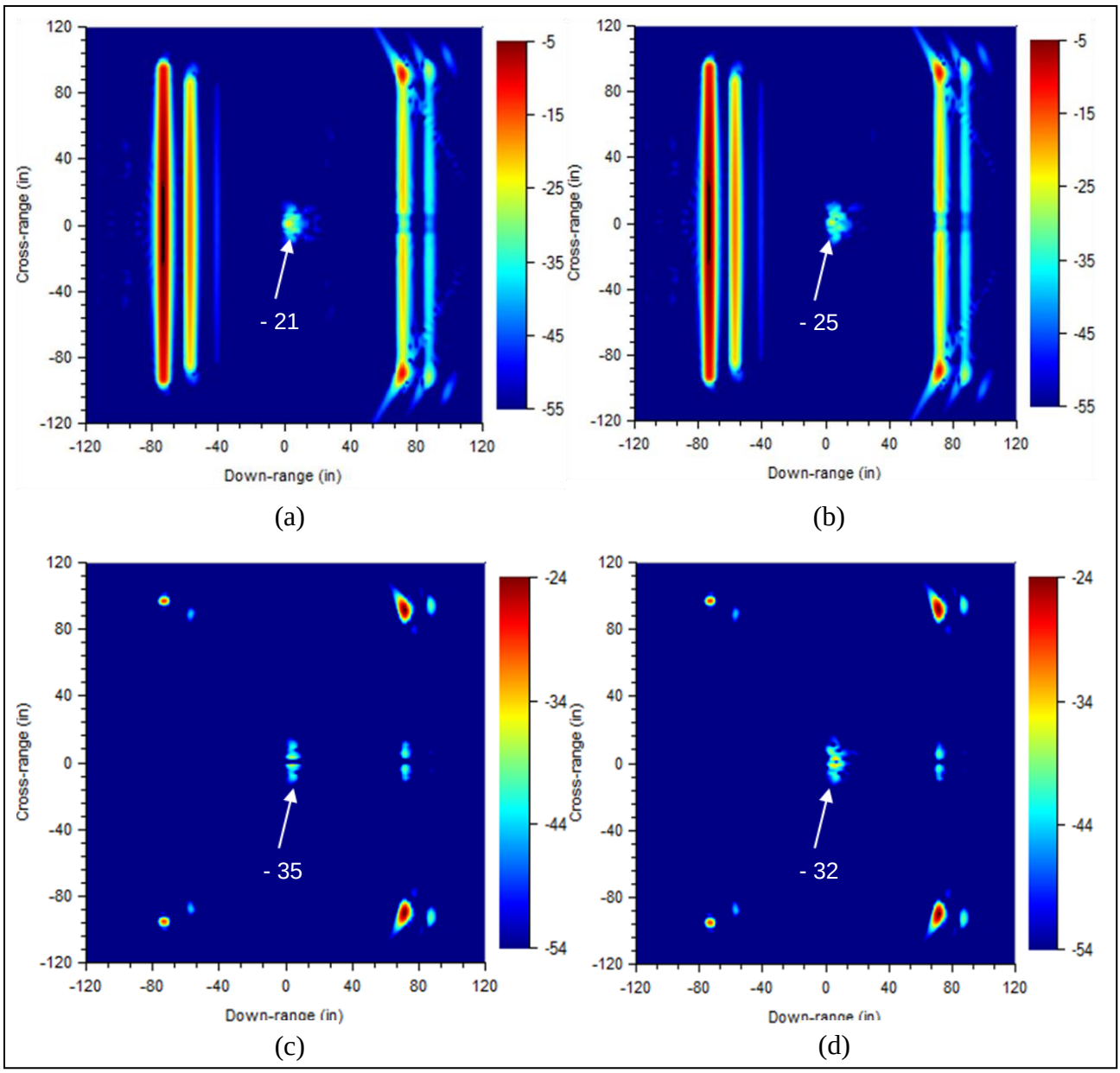

Figure 21. SAR images of the human placed in a middle of a brick wall room, including the SIRE antenna effects, showing: (a) V-V polarization, human unarmed; (b) V-V polarization, human with AK-47; (c) H-V polarization, human unarmed; and (d) H-V polarization, human with AK-47.

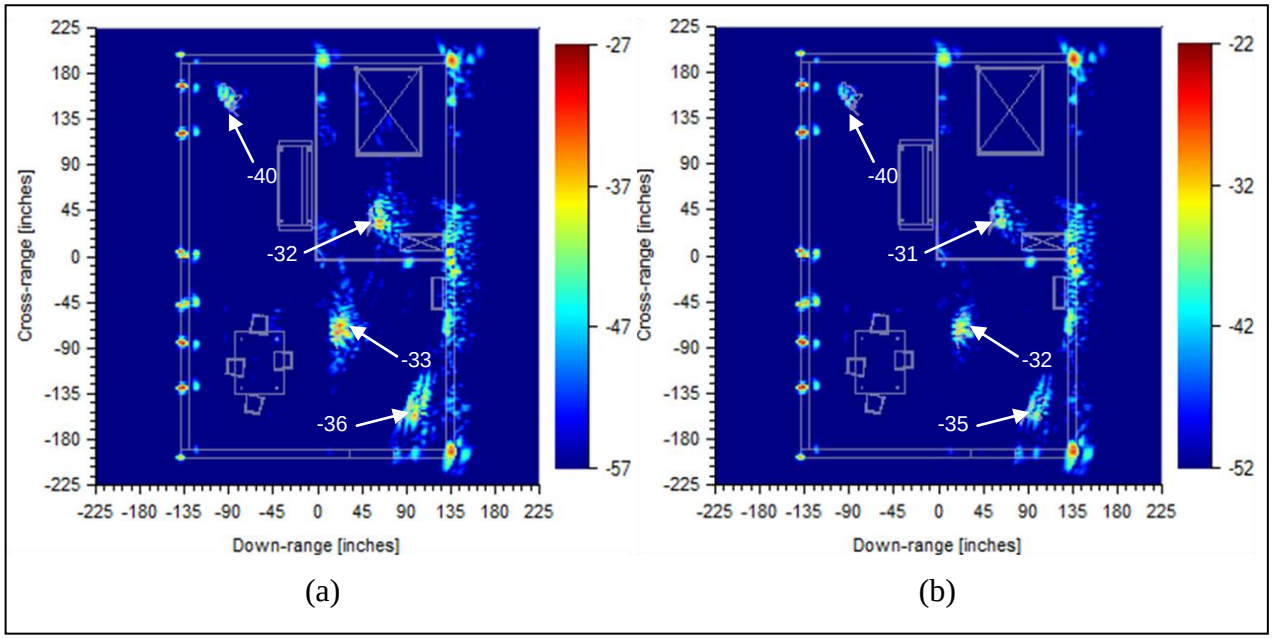

Figure 22. Cross-polarization (H-V) SAR images of the complex room, including the effects of the SIRE antennas tilted at (a) 1º in elevation and (b) 2º in elevation.

Note: In both cases, all humans carry AK-47 rifles.

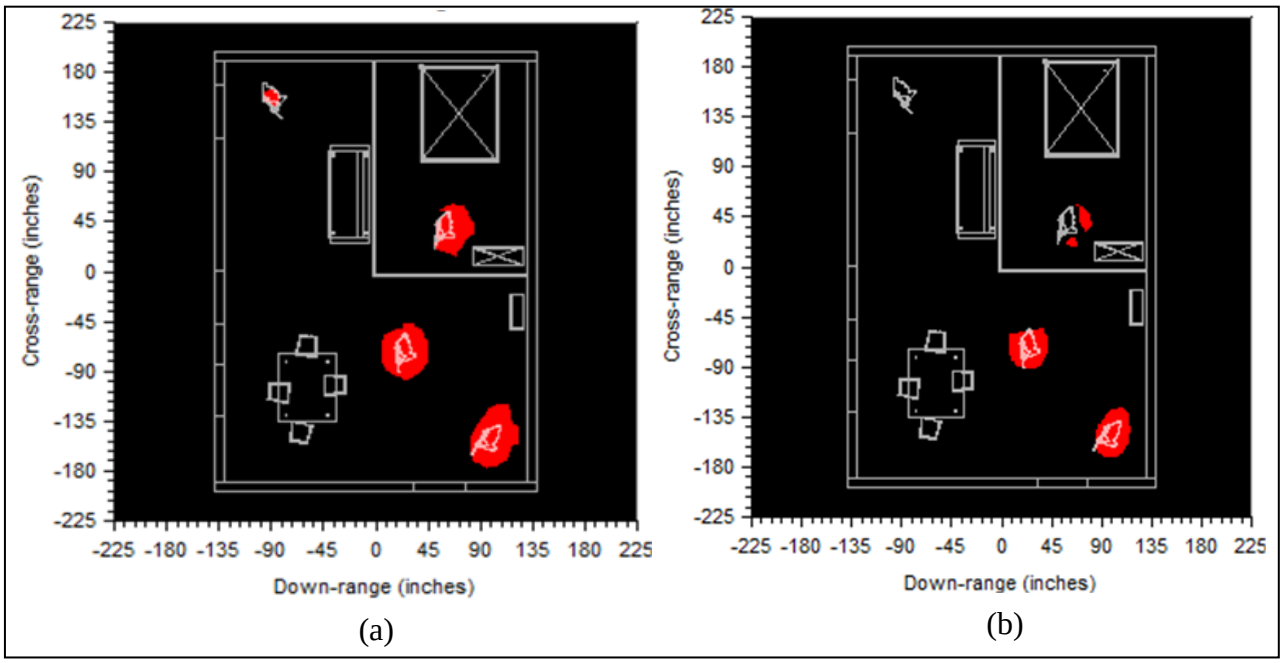

Figure 23. Detection maps for the complex room in figure 12, for a SAR system equipped with SIRE antennas tilted at (a) 1º in elevation and (b) 2º in elevation.

Note: In both cases, all humans carry AK-47 rifles.

4. Conclusions

In this study, we provided a formulation for characterizing the radar polarimetric scattering response by taking into account both the transmission/reception antenna patterns and the target radar signature. Subsequently, we applied this formulation to the problem of through-the-wall detection of small weapons based on polarimetric differences of radar images.

In section 2, we derived the polarimetric equations that relate the radar response to the antenna characteristics (via the normalized effective length vectors) and the target (via the scattering matrix). These equations can be applied to the calculation of the far-field radar response through computer models, by separating the evaluation of the antenna radiation and reception from that of the target radar signature. Compared to our previous radar performance prediction studies that were based on modeling the target signature under pure plane wave excitation and observation, the current work replaces the plane-wave-based scattering matrix **SP** by the antenna-pattern-based scattering matrix **SA** in evaluating the radar system performance. In section 2.3, we explained why considering the coupling between the polarimetric characteristics of the antenna radiation and target scattering is important in simulating an UWB, broad-beam, strip-map SAR imaging system operating at relatively low frequencies (1–4 GHz), typical for STTW applications.

In section 3, we employed this formulation to analyze the performance of a through-the-wall small weapon detection system based on polarimetric differences between SAR images. We used two different types of radar antenna systems, as well as two different scenes. By assessing the influence of the cross-polarization suppression *PR* of a simple antenna (section 3.2) on the weapon detection scheme performance, we derived an approximate lower bound for the PR_{RMS} parameter required by this technique to work. Subsequently, we repeated the analysis with FEKO-simulated patterns of the SIRE transmitting and receiving antennas.

We should mention that a number of simplifying assumptions were made in our models, many of them discussed in section 2.5. Also, the antenna patterns considered in the numerical examples in section 3 were somewhat artificial, even when they represented models of the SIRE antenna designs. One reason for using antenna pattern models rather than experimental data was the fact that complete measurements of the SIRE antenna patterns were not available to us. Additionally, the simulated SIRE antenna data went through further processing to make them more suitable for UWB pulse excitation (notice that the goal of this study was to assess the polarimetric performance, not the UWB characteristics of the antennas). Nevertheless, the technique is readily capable of mixing simulation and measurement data on both the antennas and the target.

As discussed in section 2.5, this formulation can be adapted to solve the "inverse problem" (finding the **SP** matrix based on the measured **SA** matrix), which first involves performing the

polarimetric calibration of a radar system. Notice that, in this study, we did not attempt to compensate for the polarimetric antenna effects in the final SAR images (according to equation 25). Doing so would have produced “perfect” polarimetric images (identical to those created under the plane wave assumption), since all results were obtained via computer modeling, without considering any noise or calibration errors. In practice, such “perfect” polarimetric images cannot be achieved, even after the calibration and compensation procedures. Our results are still useful to the radar system designer, by establishing an upper bound to the polarimetric performance (the plane wave transmission and reception case), as well as measuring the performance degradation when various levels of antenna cross-polarization isolation are considered.

One shortcoming of the model outlined here is that it cannot be applied to a near-field radar scattering scenario. For this purpose, a near-field EM model of the entire scene (including the antennas and the target) needs to be developed. In that case, the antenna radiation and reception and the target scattering are part of the same simulation, and must not be separated. This type of modeling will be the subject of future research.

5. References

1. Dogaru, T.; Le, C. *Through-the-Wall Small Weapon Detection Based on Polarimetric Radar Techniques*; ARL-TR-5041; U.S. Army Research Laboratory: Adelphi, MD, December 2009.

2. Balanis, C. *Advanced Engineering Electromagnetics*, Wiley: New York, 1989.

3. Nguyen, L.; Ressler, M.; Sichina, J. Sensing through the Wall Imaging Using the Army Research Lab Ultra-Wideband Synchronous Impulse Reconstruction (UWB SIRE) Radar. *Proceedings of SPIE* **2008**, *6947*.

4. Barnes, R. M. *Polarimetric Calibration Using In-Scene Reflectors*; MIT Lincoln Laboratory Project Report TT-63: Lexington, MA, September 1986.

5. Sarabandi, K.; Ulaby, F. T.; Tassoudji, M. A. Calibration of Polarimetric Radar System with Good Polarization Isolation. *IEEE Transactions on Geoscience and Remote Sensing* **January 1990**, *28* (1), 70–75.

6. Whitt, M. W.; Ulaby, F. T.; Polatin, P.; Liepa, V. V. A General Polarimetric Radar Calibration Technique. *IEEE Transactions on Antennas and Propagation* **January 1991**, *39* (1), 62–67.

7. Sarabandi, K.; Pierce, L. E.; Ulaby, F. T. Calibration of a Polarimetric Imaging SAR. *IEEE Transactions on Geoscience and Remote Sensing* **May 1992**, *30* (3), 540–549.

8. Ertin, E.; Potter, L. C. Polarimetric Calibration for Wideband Synthetic Aperture Radar Imaging. *IEE Proceedings – Radar, Sonar, Navigation* **October 1998**, *145* (5), 275–280.

9. Freeman, A.; Van Zyl, J. J.; Klein, J. D.; Zebker, H. A.; Shen, Y. Calibration of Stokes and Scattering Matrix Format Polarimetric SAR Data. *IEEE Transactions on Geoscience and Remote Sensing* **May 1992**, *30* (3), 531–539.

10. Touzi, R.; Vachon, P. W.; Wolfe, J. Requirement on Antenna Cross-Polarization Isolation for the Operational Use of C-Band SAR Constellations in Maritime Surveillance. *IEEE Geoscience and Remote Sensing Letters* **October 2010**, *7* (4), 861-865.

11. Dogaru, T.; Le, C.; Nguyen, L. *SAR Images of a Simple Room Based on Computer Models*; ARL-TR-5193; U.S. Army Research Laboratory: Adelphi, MD, May 2010.

12. Dogaru, T.; Le, C. *Through-the-Wall Radar Simulations for Complex Room Imaging*; ARL-TR-5205; U.S. Army Research Laboratory: Adelphi, MD, May 2010.

13. Dogaru, T. *AFDTD User's Manual*; ARL-TR-5145; U.S. Army Research Laboratory: Adelphi, MD, March 2010.

14. Taflove, A.; Hagness, S. C. *Computational Electrodynamics: The Finite-Difference Time-Domain*, Artech House: Boston, MA, 2000.

15. Soumekh, M. *Synthetic Aperture Radar Signal Processing*, Wiley: New York, 1999.

16. Oppenheim, A. V.; Schafer, R. W. *Discrete-Time Signal Processing*, Prentice Hall: Englewood Cliffs, NJ, 1989.

17. Carrara, W.; Goodman, R.; Majewski, R. *Spotlight Synthetic Aperture Radar – Signal Processing Algorithms*, Artech House: Boston, MA, 1995.

18. Munson, D. C.; O'Brien, J. D.; Jenkins, W. K. A Tomographic Formulation of Spotlight-Mode Synthetic Aperture Radar. *Proceeings of the IEEE* **August 1983**, *71* (8), 917–925.

19. Mott, H. *Remote Sensing with Polarimetric Radar*, Wiley-Interscience: Hoboken, NJ, 2007.

20. Balanis, C. *Antenna Theory – Analysis and Design*, Wiley: New York, 1997.

21. Ruch, G.; Barrick, D. E.; Stuart, W. D.; Krichbaum, C. K. *Radar Cross Section Handbook*, Plenum Press, New York, 1970.

22. Smith, G. D.; Harris, R. W.; Ressler, M.; Stanton, B. *Wideband Vivaldi Notch Antenna Design for UWB SIRE VHF/UHF Radar*; ARL-TR-4409; U.S. Army Research Laboratory: Adelphi, MD, November 2006.

23. Science Applications International Corporation (SAIC) Web page. http://www.saic.com/products/software/xpatch (accessed December 2009).

24. Yu, C. L.; Kipp, R.; Andersh, D. J.; Lee, S. W. Near-Field Electromagnetic Modeling and Analysis. *1997 IEEE Antennas Propagation International Symposium* **July 1997**, *2*, 1168–1171.

25. Le, C.; Nguyen, L.; Dogaru, T. Radar Imaging of a Large Building based on Near-Field Xpatch Model. *2010 IEEE Antennas Propagation International Symposium* **July 2010**.

26. ARL MSRC Web page. http://www.arl.hpc.mil (accessed August 2011).

27. FEKO EM Simulation Software Web page. http://www.feko.info (accessed October 2011).

28. EM Software & Systems. *FEKO User's Manual, Suite 6.1*; Stellenbosch, South Africa, July 2011.

29. Dogaru, T.; Nguyen, L.; Le, C. *Computer Models of the Human Body Signature for Sensing Through the Wall Radar Applications*; ARL-TR-4290; U.S. Army Research Laboratory: Adelphi, MD, September 2007.

30. Ressler, M.; Nguyen, L.; Koenig, F.; Wong, D.; Smith, G. D. The Army Research Laboratory (ARL) Synchronous Impulse Reconstruction (SIRE) Forward-Looking Radar. *Proceedings of SPIE* **2007**, *6561*.

31. Kenyon, C. *Optimization of a Resistively-Loaded Antenna Using FEKO Software*; ARL-TR-4633; U.S. Army Research Laboratory: Adelphi, MD, November 2008.

List of Symbols, Abbreviations, and Acronyms

2-D	two-dimensional
3-D	three-dimensional
ARL	U.S. Army Research Laboratory
BPA	back-projection algorithm
CEM	computational electromagnetics
DSRC	Defense Supercomputing Resource Center
EM	electromagnetic
H-V	horizontal-vertical
HPC	high-performance computing
PFA	polar format algorithm
RCS	radar cross section
RF	radio frequency
RMS	root mean square
SAR	synthetic aperture radar
SIRE	Synchronous Impulse Reconstruction
STTW	sensing through the wall
TEM	transversal electromagnetic
UWB	ultra-wideband
V-V	vertical-vertical

NO. OF COPIES	ORGANIZATION
1 PDF	ADMNSTR DEFNS TECHL INFO CTR ATTN DTIC OCP 8725 JOHN J KINGMAN RD STE 0944 FT BELVOIR VA 22060-6218
1	US ARMY RSRCH DEV & ENGRG CMND ARMAMENT RSRCH DEV & ENGRG CTR ARMAMENT ENGRG & TECHNLGY CTR ATTN AMSRD AAR AEF T J MATTS BLDG 305 APG MD 21005-500
1	US ARMY TRADOC BATTLE LAB INTEGRATION & TECHL DIRCTRT ATTN ATCH B 10 WHISTLER LANE FT MONROE VA 23651-5850
2	US ARMY RDECOM CERDEC I2WD ATTN RDER IWI MS J CUA BLDG 6003 COMBAT DRIVE APG MD 21005
1	US ARMY INFO SYS ENGRG CMND ATTN AMSEL IE TD A RIVERA FT HUACHUCA AZ 85613-5300
1	US GOVERNMENT PRINT OFF DEPOSITORY RECEIVING SECTION ATTN MAIL STOP IDAD J TATE 732 NORTH CAPITOL ST NW WASHINGTON DC 20402

NO. OF COPIES	ORGANIZATION
16	US ARMY RSRCH LAB ATTN RDRL D ATTN RDRL CIO LT TECHL PUB ATTN RDRL CIO LL TECHL LIB ATTN AMSRD ARL SE RM W O COBURN ATTN AMSRD ARL SE RU A SULLIVAN ATTN AMSRD ARL SE RU C LE ATTN AMSRD ARL SE RU L NGUYEN ATTN AMSRD ARL SE RU D LIAO ATTN AMSRD ARL SE RU C KENYON ATTN AMSRD ARL SE RU K RANNEY ATTN AMSRD ARL SE RU A MARTONE ATTN AMSRD ARL SE RU K KAPPRA ATTN AMSRD ARL SE RU M RESSLER ATTN AMSRD ARL SE RU T DOGARU (2 COPIES) ATTN IMNE ALC HRR MAIL & RECORDS MGMT ADELPHI MD 20783-1197

TOTAL: 23 (1 ELEC, 22 HCS)

INTENTIONALLY LEFT BLANK.